

FINAL TECHNICAL REPORT
(Covered the period from June 1, 1998 to May 31, 2000)
Grant number: DAAG55-98-1-0325

**INVESTIGATION OF MULTICOLOR AND SIMPLIFIED
QUANTUM WELL INFRARED PHOTODETECTORS FOR MWIR
AND LWIR DETECTION**

Submitted to

U.S. ARMY RESEARCH OFFICE

P. O. Box 12211
Research Triangle Park NC 27709

Prepared by

Sheng S. Li, Professor

Dept. of Electrical and Computer Engineering
University of Florida
Gainesville, FL 32611-6130
Tel/fax: 352-392-4937
Email: shengli@eng.ufl.edu

June 1, 2000

**APPROVED FOR PUBLIC RELEASE;
DISTRIBUTION UNLIMITED.**

**THE VIEWS, OPINIONS, AND/OR FINDINGS CONTAINED IN THIS REPORT
ARE THOSE OF THE AUTHOR(S) AND SHOULD NOT BE CONSTRUED AS
AN OFFICIAL DEPARTMENT OF THE ARMY POSITION, POLICY, OR
DECISION, UNLESS SO DESIGNATED BY OTHER DOCUMENTATION.**

FINAL TECHNICAL REPORT
(Covered the period from June 1, 1998 to May 31, 2000)
Grant number: DAAG55-98-1-0325

**INVESTIGATION OF MULTICOLOR AND SIMPLIFIED
QUANTUM WELL INFRARED PHOTODETECTORS FOR MWIR
AND LWIR DETECTION**

Submitted to

U.S. ARMY RESEARCH OFFICE

**P. O. Box 12211
Research Triangle Park NC 27709**

Prepared by

Sheng S. Li, Professor

**Dept. of Electrical and Computer Engineering
University of Florida
Gainesville, FL 32611-6130
Tel/fax: 352-392-4937
Email: shengli@eng.ufl.edu**

June 1, 2000

**APPROVED FOR PUBLIC RELEASE;
DISTRIBUTION UNLIMITED.**

**THE VIEWS, OPINIONS, AND/OR FINDINGS CONTAINED IN THIS REPORT
ARE THOSE OF THE AUTHOR(S) AND SHOULD NOT BE CONSTRUED AS
AN OFFICIAL DEPARTMENT OF THE ARMY POSITION, POLICY, OR
DECISION, UNLESS SO DESIGNATED BY OTHER DOCUMENTATION.**

REPORT DOCUMENTATION PAGE

Form Approved
OMB NO. 0704-0188

Public Reporting burden for this collection of information is estimated to average 1 hour per response, including the time for reviewing instructions, searching existing data sources, gathering and maintaining the data needed, and completing and reviewing the collection of information. Send comment regarding this burden estimate or any other aspect of this collection of information, including suggestions for reducing this burden, to Washington Headquarters Services, Directorate for Information Operations and Reports, 1215 Jefferson Davis Highway, Suite 1204, Arlington, VA 22202-4302, and to the Office of Management and Budget, Paperwork Reduction Project (0704-0188), Washington, DC 20503.

1. AGENCY USE ONLY (Leave Blank)		2. REPORT DATE June 5, 2000	3. REPORT TYPE AND DATES COVERED Final Report 06/01/98 - 05/31/00
4. TITLE AND SUBTITLE Investigation of Multicolor and Simplified Quantum Well Infrared Photodetectors for MWIR and LWIR Detection		5. FUNDING NUMBERS DAAG55-98-1-0325	
6. AUTHOR(S) Sheng S. Li, Professor		8. PERFORMING ORGANIZATION REPORT NUMBER	
7. PERFORMING ORGANIZATION NAME(S) AND ADDRESS(ES) University of Florida Gainesville, FL 32611-6130		10. SPONSORING / MONITORING AGENCY REPORT NUMBER ARO 28853.6-EL	
9. SPONSORING / MONITORING AGENCY NAME(S) AND ADDRESS(ES) U. S. Army Research Office P.O. Box 12211 Research Triangle Park, NC 27709-2211		11. SUPPLEMENTARY NOTES The views, opinions and/or findings contained in this report are those of the author(s) and should not be construed as an official Department of the Army position, policy or decision, unless so designated by other documentation.	
12 a. DISTRIBUTION / AVAILABILITY STATEMENT Approved for public release; distribution unlimited.		12 b. DISTRIBUTION CODE	
13. ABSTRACT (Maximum 200 words) In this research program, we have investigated a four-stack, four-color quantum well infrared photodetector (QWIP), and studied the voltage distribution and temperature effect in this four-color QWIP. We have conducted a study on the quantum confined Stark-effect in an n-type QWIP. We have performed theoretical studies of the intersubband optical transitions in quantum dots and the design of GaAs/InGaAs and InAs/InAlAs quantum dot infrared photodetectors (QDIPs) for MWIR and LWIR detection. A new QWIP for very long wavelength infrared (VLWIR) applications has been investigated for 14-16 μm detection. Specific issues concerning device physics, detector design and device performance of the VLWIR QWIP are addressed. A VLWIR QWIP has been designed, fabricated and characterized. Two high performance multi-color, broadband QWIPs using digital graded superlattice barriers (DGS LB) for long wavelength infrared (LWIR) and broadband (BB) infrared detection have been demonstrated. We have also developed a high performance broadband (BB) $\text{In}_{0.26}\text{Ga}_{0.74}\text{As}/\text{Al}_x\text{Ga}_{1-x}\text{As}$ QWIP using a linearly graded (LGB) $\text{Al}_x\text{Ga}_{1-x}\text{As}$ barrier for LWIR detection. Theoretical study on the enhancement of quantum efficiency in a QWIP by using photonic crystal structure has also been carried out in this report.			
14. SUBJECT TERMS N-type quantum well infrared photodetectors (QWIPs), multi-stack, quantum well multi-color, quantum dot, very long wavelength (VLWIR), Stark shift, digital graded superlattice barrier, linear-graded barrier.		15. NUMBER OF PAGES 77	
17. SECURITY CLASSIFICATION OR REPORT UNCLASSIFIED		16. PRICE CODE	
18. SECURITY CLASSIFICATION ON THIS PAGE UNCLASSIFIED	19. SECURITY CLASSIFICATION OF ABSTRACT UNCLASSIFIED	20. LIMITATION OF ABSTRACT UL	

NSN 7540-01-280-5500

Standard Form 298 (Rev.2-89)
Prescribed by ANSI Std. Z39-18
298-102

TABLE OF CONTENTS

	Page
1. Voltage Distribution and Temperature Effect in a Four-color Quantum Well Infrared Photodetector	3
1.1 Introduction.....	3
1.2 Measured Temperature Effect in the Four-color QWIP	5
1.3 Explanation of Temperature Effect in the Four-color QWIP	5
1.3.1 <u>General Considerations</u>	5
1.3.2 <u>Calculated Results</u>	8
1.4 Conclusions.....	11
1.5 References.....	11
2. Experimental Study on the Stark-effect and a Broadband QWIP.....	12
2.1 The Stark-effect QWIP	12
2.1.1 <u>The Device Structure</u>	13
2.1.2 <u>The Dark current</u>	13
2.1.3 <u>The Responsivity</u>	13
2.1.4 <u>Discussions</u>	14
2.2 The Broadband QWIP.....	15
2.2.1 <u>The Device Structure</u>	15
2.2.2 <u>The Dark Current</u>	16
2.2.3 <u>The Responsivity</u>	17
2.2.4 <u>Discussions</u>	18
2.3 Reference	18
3. Study of Intersubband Transition in Quantum Dots and Quantum Dot Infrared Photodetectors.....	19
3.1 Introduction.....	19
3.2 Theoretical Consideration.....	20
3.3 Results and Discussion	23
3.4 Conclusions.....	32
3.5 References.....	32
4. Very-Long-Wavelength Quantum Well Infrared Photodetectors.....	35
4.1 Introduction.....	35
4.2 Design Consideration of VLWIR QWIPs.....	37
4.2.1 <u>Blackbody Radiation</u>	38
4.2.2 <u>The Dark Current and Dynamic Resistance</u>	39
4.2.3 <u>The Detectivity</u>	41
4.2.4 <u>The Peak Wavelength Shift due to Exchange Interaction</u>	42
4.3 VLWIR QWIP in a Multicolor QWIP Stack	44
4.4 A 14.7 μm VLWIR QWIP	45
4.5 Conclusions.....	49
4.6 References.....	49

5. Quantum-Well Infrared Photodetectors With Digital Graded Superlattice Barrier For Long Wavelength and Broadband Detection	51
5.1 Introduction.....	51
5.2 Device Design and Fabrication.....	51
5.3 Results and Discussions	53
5.4 Conclusions.....	58
5.5 References.....	58
6. Multi-color, Broadband Quantum Well Infrared Photodetectors With Linear-Graded Barrier	60
6.1 Introduction.....	60
6.2 Device Design and Fabrication.....	60
6.3 Results and Discussions	61
6.4 Conclusions.....	66
6.5 References.....	66
7. Enhancing the Quantum Efficiency of a QWIP by using Photonic Crystal (PC) Structure.....	67
7.1 Introduction.....	67
7.2 Theoretical Consideration.....	68
7.2.1 Reflecting and Refracting Through a Multi-layer Film	68
7.2.2 Grating Coupler.....	69
7.3 Results.....	73
7.3.1 Transmission Coefficient of a PC structure	73
8. Publications.....	75

1. Voltage Distribution and Temperature Effect in a Four-color Quantum Well Infrared Photodetector

1.1 Introduction

We have combined the stacked multicolor structure with the simplified quantum well infrared photodetector (S-QWIP) concept, and designed and processed a four-color QWIP [1]. The four-color QWIP consists of four stacks of multiple QWs. The bottom two stacks consist of eight periods of 600 Å $\text{Al}_{0.27}\text{Ga}_{0.73}\text{As}$ barriers and 55 Å GaAs wells, and four periods of 400 Å $\text{Al}_{0.38}\text{Ga}_{0.62}\text{As}$ barriers and 35 Å $\text{In}_{0.22}\text{Ga}_{0.78}\text{As}$ wells, which have peak detection wavelengths at 8.5 μm and 4.7 μm, respectively. The doping densities in the 8.5 μm and 4.7 μm stacks are $7 \times 10^{17} \text{ cm}^{-3}$ and $2.8 \times 10^{18} \text{ cm}^{-3}$, respectively. The top two stacks consist of five periods of 500 Å $\text{Al}_{0.25}\text{Ga}_{0.75}\text{As}$ barriers and 50 Å GaAs wells, and ten periods of 800 Å $\text{Al}_{0.16}\text{Ga}_{0.84}\text{As}$ barriers and 65 Å GaAs wells, which have the response peaks at 9 μm, and 12.3 μm, respectively. The doping densities in the 9 μm and 12.3 μm stacks are $0.6 \times 10^{18} \text{ cm}^{-3}$ and $0.4 \times 10^{18} \text{ cm}^{-3}$, respectively. A contact layer with doping density of $1 \times 10^{18} \text{ cm}^{-3}$ is grown between the top and the bottom two stacks. The whole structure was sandwiched between the top and bottom contact layers with a doping density of $1 \times 10^{18} \text{ cm}^{-3}$. A schematic energy band diagram of this four-stack QWIP is shown in figure 1.1. By using different number of QWs of less than 10 periods in each stack, different barrier width and doping density in each stack, the voltage tuning among the four stacks was successfully achieved without requiring to apply a very high bias voltage to the device. Four different combinations of the two-color detection can be achieved simultaneously. Adding two extra contacts to separate each stack makes simultaneous reading of four colors possible if the read-out integrated circuits (ROICs) and indium bump technology are available. The detector can also be used as a voltage

tunable multicolor detector by using only the top and bottom stacks. The results of this new design demonstrate the flexibility of QWIP in achieving different detection wavelengths, voltage tunability, and multicolor capabilities.

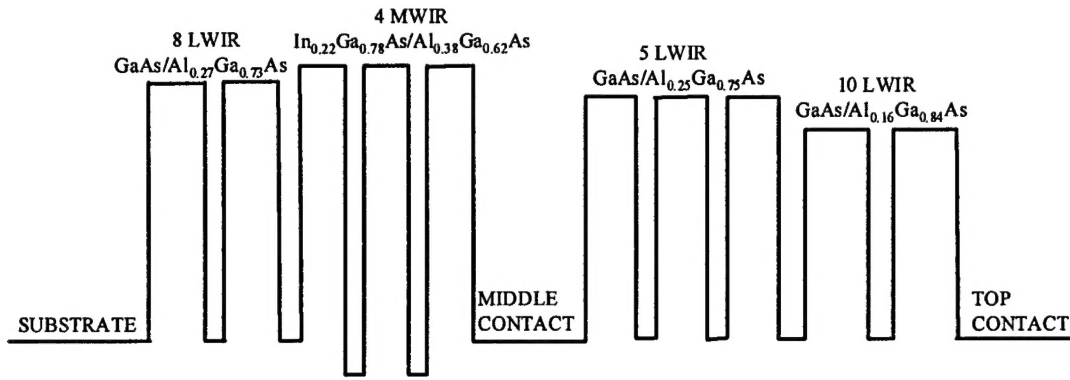


Figure 1.1 Schematic energy band diagram for the four-stack four-color QWIP.

In the multi-stack QWIP, an important issue is the temperature effect and the distribution of bias voltage among the multi-stacks. In the short period QWIPs, the temperature effect is quite significant [2,3]. The voltage distribution and temperature effect are also very important in our four-color simplified QWIP. We will investigate this problem in this chapter.

1.2 Measured Temperature Effect in the Four-color QWIP

Figure 1.2 shows the temperature dependence of the peak responsivity for (a) the top stack and (b) the bottom stack. For the top stack, as the temperature increases from 40 K to 77 K, there is a significant decrease in the responsivity of 12.3 μm stack, and in fact the responsivity of 12.3 μm stack becomes almost unobservable at 77 K. On the other hand, there is a very large increase in the responsivity for the 9 μm stack. For example, at $V_b = 0.8$ V, the peak responsivity of the 9 μm stack increases from 0.16 A/W at 40 K to

1.11 A/W at 77 K, which is seven times of the corresponding peak responsivity at 40 K. From figure 1.2(b) one can find that as temperature increases from 40 K to 77 K, both the peak responsivity of 4.7 μm and 8.5 μm stacks increased. The enhancement is quite significant, for example, at bias of 2.5 V, the responsivity of the 4.7 μm stack increases from 0.20 A/W at 40 K to 0.51 A/W at 77 K, the responsivity of the 8.5 μm stack increases from 0.14 A/W at 40 K to 0.44 A/W at 77 K. The significant temperature effect were also observed in other short period QWIPs [2,3].

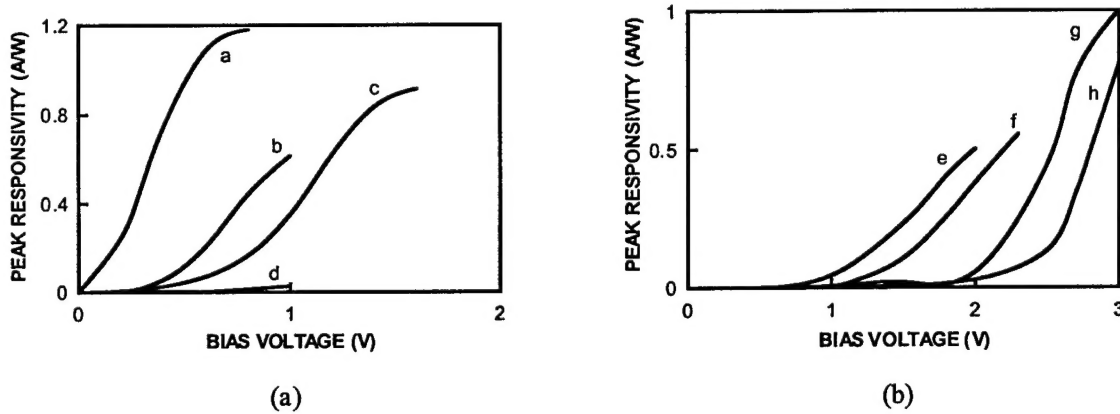


Figure 1.2 Observed temperature effect on the peak responsivity of the top two stacks (a), and the bottom two stacks (b). Curve a: 9 μm peak, 77 K; b: 12.3 μm , 40 K; c: 9 μm , 40 K; d: 12.3 μm , 77 K. Curve e: 4.7 μm , 77 K; f: 4.7 μm , 40 K; g: 8.5 μm , 77 K; h: 8.5 μm , 40 K.

1.3 Explanation of Temperature Effect in the Four-color QWIP

1.3.1 General Considerations

We have performed theoretical calculations of the dark current and impedance of each stack composing of the four-color QWIP and used the results to explain the observed dependence of responsivities on bias and temperature.

Several dark current models have been developed [4,5,6,7]. The model in ref. [4] is relatively simple and shows clear physical meaning, and it accounts for the thermionic emission (TE) and thermally- assisted tunneling (TAT). Calculated result using this

model agrees well with experiment in a QWIP in which the dominant dark current mechanism is TE and TAT. The other models are more sophisticated and provide an excellent description of the current-voltage characteristics of QWIP under low electric field condition.

The dark current I_D of a QWIP can be expressed as [4]

$$I_D = \frac{e m_w^* A}{\pi \hbar L_p^2} \frac{\mu F}{\sqrt{1 + (\mu F / v_s)^2}} \int_{E_1}^{\infty} f(E) T(E, F) dE \quad (1.1)$$

where e is the electronic charge, m_w^* is the electron effective mass in the QW, A is the device area, L_p is the QWIP period length, μ is the electron mobility, F is the electric field inside the QWIP, v_s is the electron saturation velocity, $f(E)$ is the Fermi-Dirac distribution function, and $T(E, F)$ is the bias-dependent tunneling current transmission coefficient for a single barrier.

Assuming that L_w is the well width, L_b the barrier width, m_b^* the electron effective mass in the barrier and E_b the barrier height, then under an applied field F , the tunneling probability can be obtained from the WKB approximation, and the result yields

$$T(E, F) = \begin{cases} 1, & E > E_b - eF L_w \\ \exp\left(-\frac{4}{3\hbar e F} (2m_b^*)^{1/2} (E_b - E - eF L_w)^{3/2}\right), & E_b - eF(L_w + L_b) < E < E_b - eF L_w \\ \exp\left(-\frac{4}{3\hbar e F} (2m_b^*)^{1/2} \left\{ (E_b - E - eF L_w)^{3/2} - (E_b - E - eF(L_w + L_b))^{3/2} \right\}\right), & E_1 < E < E_b - eF(L_w + L_b) \end{cases} \quad (1.2)$$

By solving for $T(E, F)$, it is straightforward to calculate the dark current I_D and the dynamic impedance Z of a single period QWIP (i.e., $Z = dV/dI_d$).

In ref. [6] by taking into account the electric field effect and the Schottky image effect, the dark current is formulated as

$$I = I_0 \exp\left(\frac{e\Delta\phi + eF_w L_w}{kT}\right) \left[1 - \exp\left(-\frac{eV_b}{kT}\right)\right] \quad (1.3)$$

where I_0 is the thermally generated current in equilibrium, e is the electron charge, $\Delta\phi$ is the image-force-induced barrier lowering, F_w is the electric field in the well and L_w is the well width, k is the Boltzmann constant, T is the temperature. In this dark current model the QWIP is thought of as consisting of M (the ratio of the active device length over the extended state carrier trajectory), statistically independent sections each made up of a barrier region with two doped quantum wells as contacts from which the carriers are emitted, V_b is the voltage drop across a single section. $\Delta\phi$ is given by

$$\Delta\phi = \sqrt{\frac{eF_b}{4\pi\epsilon_0\epsilon_b}} \quad (1.4)$$

where F_b is the electric field in the barrier, ϵ_0 is the free space permittivity and ϵ_b is the dielectric constant of barrier.

I_0 can be obtained as

$$I_0 = \frac{NkT}{eR_0} \quad (1.5)$$

where R_0 is the dynamic resistance in equilibrium.

In the calculation, the dark current at 40 K was calculated by model [6] and the dark current at 77 K was calculated by model [4]. R_0 was chosen as 10^{10} and $10^9 \Omega$ for the $\lambda_p=9 \mu\text{m}$ and $\lambda_p=12.3 \mu\text{m}$ stack, respectively at 40 K. The electron mobility and saturated velocity for the LWIR QWIP were taken as $1100 \text{ cm}^2 \cdot \text{V}^{-1}\text{s}^{-1}$ and $5 \times 10^6 \text{ cm/s}$ respectively at 77 K.

The two stacks with different peak wavelengths composing of the top stack can be approximately considered as in series, and the two stacks have the same dark current. The

total voltage applied on the top stack is distributed between these two stacks. This criterion is also applied to the bottom stack.

1.3.2 The Calculated Results

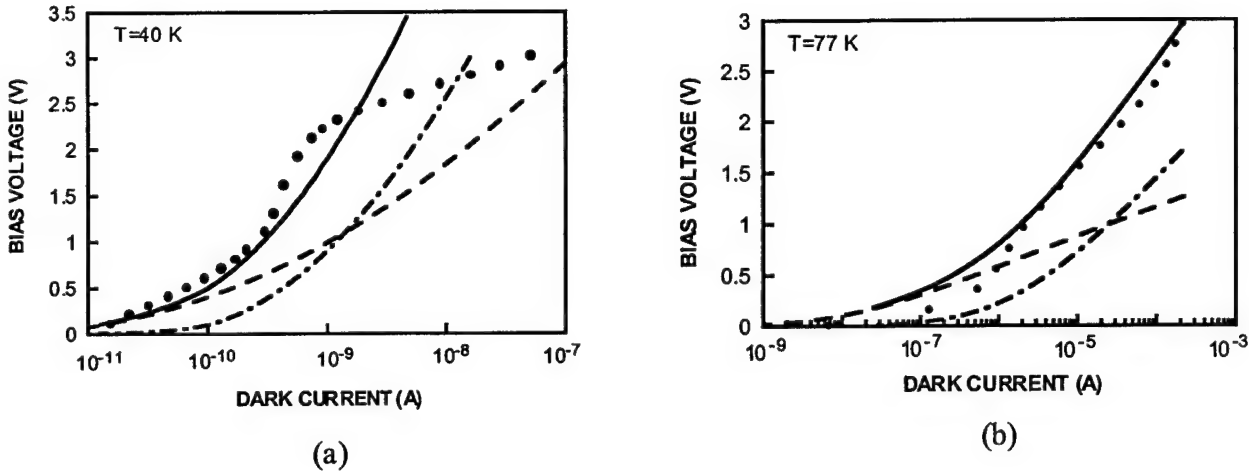


Figure 1.3 The measured and calculated bias voltages versus dark current of the top two stacks for the $\lambda_p = 9\text{ }\mu\text{m}$ and $\lambda_p = 12.3\text{ }\mu\text{m}$ peaks at 40 K (a) and 77 K (b). Solid circle is measured, and solid line is calculated; dashed and dash-dotted lines are calculated for the 9 μm and 12.3 μm stacks, respectively.

Figure 1.3 shows the measured dark current of the top two stacks and the calculated dark current of both ($\lambda_p = 9\text{ }\mu\text{m}$ and $12.3\text{ }\mu\text{m}$) stacks at (a) 40 K and (b) 77 K. In figure 1.3, the solid dots represent the measured dark $V - I_d$ values, the dashed and dash-dotted lines are the calculated $V - I_d$ for the 9 μm and 12.3 μm stacks, respectively, and the solid line is the sum of the two stacks. Since the two LWIR stacks are in series, the sum of the calculated voltage drops across these two stacks should be equal to the applied bias at each corresponding dark current. For example, at 40 K and $I_d = 10^{-10}\text{ A}$, the total applied bias is 0.6 V, while the calculated voltage drop across the 9 μm stack is 0.4 V and equals 0.1 V on the 12.3 μm stack. At 77 K and $I_d = 10^{-5}\text{ A}$, the applied bias is

1.6V, while the calculated voltage drops are 0.875 V and 0.72 V for the 9 μm and 12.3 μm stacks, respectively; the sum of the calculated voltage drops is exactly equal to the applied bias in this case. Figure 1.4 (a) and (b) show the calculated dynamic impedance for the 9 μm and 12.3 μm stacks at 40K and 77K, respectively.

As can be seen in figure 1.3 that the voltage drop on the $\lambda_p=12.3 \mu\text{m}$ QWIP is relatively small at both 40 K and 77 K when the bias is very small. This can be understood from the variation of dynamic impedance with applied bias, as shown in figure 1.4. At very low bias the dynamic impedance of the 9 μm stack is very large, and the voltage drop is mainly on this stack. With the increase of total bias, the dark current increases and the dynamic impedance of the 9 μm stack decreases, and part of the bias voltage drop begins to show up on the 12.3 μm stack, and this stack is turned on. As can be seen from figure 10 that in the operation range of $I_d \geq 10^{-9}$ A at 40 K and $\geq 10^{-6}$ A at 77 K, the dynamic impedance of the $\lambda_p=9 \mu\text{m}$ and $\lambda_p=12.3 \mu\text{m}$ stacks are comparable to each other, and hence each stack will have a reasonable voltage drop on it. As a result, simultaneous detection of two peak wavelengths can be realized in this device, as was shown in our experiment. This also confirms our design consideration to balance the impedance of the two stacks by using different QW periods in each stack of this multi-stack QWIP device.

As the temperature increases from 40 K to 77 K, a drastic increase in the dark current is expected as the thermionic emission current becomes dominant. As a result, the bias needed to obtain the same dark current at 77 K is much smaller than that at 40 K. One would expect a very large increase in the responsivity of both stacks when the temperature is increased from 40 K to 77 K. Indeed, we observed a large responsivity increase with temperature for the $\lambda_p=9 \mu\text{m}$ stack, as can be seen from figure 1.4(a). On

the other hand, the responsivity of the $\lambda_p = 12.3 \mu\text{m}$ peak decreases very fast at 77 K and is almost undetectable when bias is beyond 1 V. This can be explained as following. The probability of an electron tunneling out of the well is proportional to $\exp[-(E_b - E_F - eV_w)/kT]$, where $E_b = 0.1367 \text{ eV}$ and $E_F = 0.0431 \text{ eV}$ are the barrier height and Fermi energy, respectively; V_w is the voltage drop on a single well, k is the Boltzmann constant, and T is the temperature. Since the quantum well of the $\lambda_p = 12.3 \mu\text{m}$ stack is much shallower than that of the $\lambda_p = 9 \mu\text{m}$ stack, the increase of temperature strongly enhances the tunneling probability of the electrons in this stack. As a result, electrons in the $\lambda_p = 12.3 \mu\text{m}$ stack could be totally depleted when large bias is applied to it. Therefore we expect the photoresponse of $\lambda_p = 12.3 \mu\text{m}$ stack be seen only at small bias range at 77 K and will disappear under larger bias. This is consistent with the result of Figure (8), from which one can see the photoresponse of this stack at 77 K is extremely small and will not be able to be seen after 1 V. The small increase of photoresponse from 0 to 1 V is due to the increase of transport velocity with bias. On the other hand, almost all the voltage drop is on the $9 \mu\text{m}$ stack, which in turn greatly increases the responsivity of the $9 \mu\text{m}$ stack.

The voltage distribution and temperature effect in the bottom can be analyzed and understood in a similar way as the top stack presented above. The difference is that at 77 K the dark current of the $8.5 \mu\text{m}$ stack is not very large and hence the responsivity increase in the $8.5 \mu\text{m}$ stack was still observed. At the same time, since the voltage is quite evenly distributed on the two stacks, the responsivity of the $\lambda_p = 4.7 \mu\text{m}$ stack does not increase as dramatically as that of the $9 \mu\text{m}$ stack in the top stack, when temperature increases from 40 K to 77 K. We conclude that the responsivity of each stack in a two-stack QWIP depends not only on the bias voltage and temperature but also on the peak detection wavelengths of the two stacks.

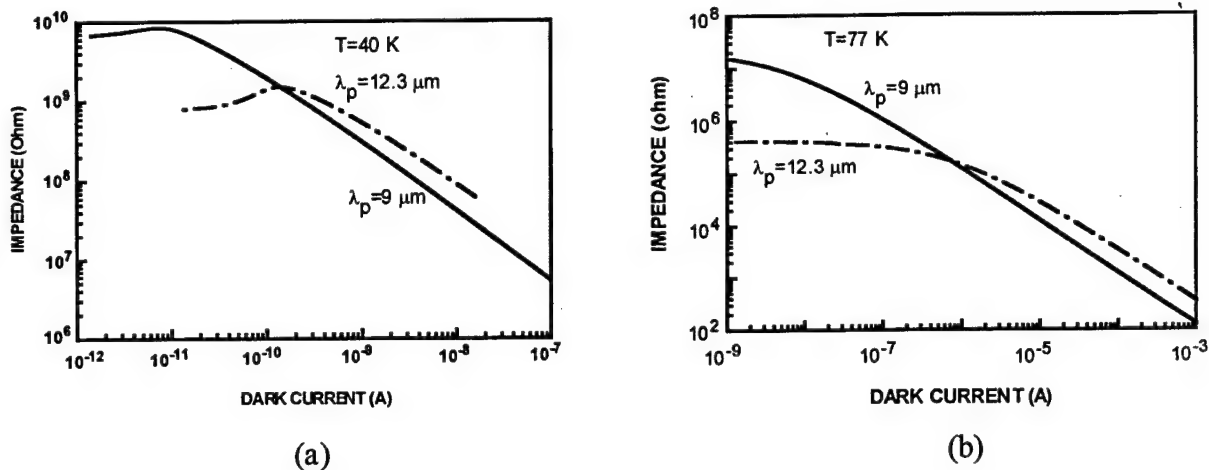


Figure 1.4 Calculated dynamic impedance versus dark current of the $\lambda_p=9\text{ }\mu\text{m}$ and $\lambda_p=12.3\text{ }\mu\text{m}$ stacks at 40 K (a) and 77 K(b).

The voltage distribution and temperature effect in the bottom and whole stacks can be explained in a similar way as in the case of the top two stacks given above

1.4 Conclusions

The four-stack, four-color QWIP exhibits significant temperature effect, and the voltage distribution among these stacks are rather complicated. Our calculation of dark current and dynamical impedance for each stack can be used to semi-quantitatively understand these phenomena. The theoretical calculation also confirms our considerations for the design of using different periods for different stacks to balance the impedances of these stacks, and therefore to realize simultaneous multi-color detection.

1.5 References

1. M.Z. Tidrow, Xudong Jiang, Sheng S. Li and K. Bacher, Appl. Phys. Lett. **74**, 1335 (1999).

2. J.C. Chiang, Sheng S. Li, M.Z. Tidrow, P. Ho, M. Tsai and C.P. Lee, Appl. Phys. Lett. **69**, 2412 (1996).
3. M.Z. Tidrow and K. Bacher, Appl. Phys. Lett. **69**, 3396 (1996).
4. B.F. Levine, C.G. Bethea, G. Hasnain, V.O. Shen, E. Pelve, R.R. Abbott and S.J. Hsieh, Appl. Phys. Lett. **56**, 851 (1990).
5. L. Thibaudeau, P. Bois and J.Y. Duboz, J. Appl. Phys. **79**, 446 (1996).
6. D.C. Wang, G. Bosman and S.S. Li, Appl. Phys. Lett. **68**, 2532 (1996).
7. V. Ryzhii, J. Appl. Phys. **81**, 6442 (1997).

2. Experimental Study on the Stark-effect and a Broadband QWIP

2.1 The Stark-Effect QWIP

2.1.1 The Device Structure

We have designed an asymmetric weakly coupled double quantum wells structure to study the quantum confined Stark effect and use this effect to tune the peak wavelength of the QWIP made of this structure, the schematic energy band diagram of this double wells structure is shown in figure 2.1.

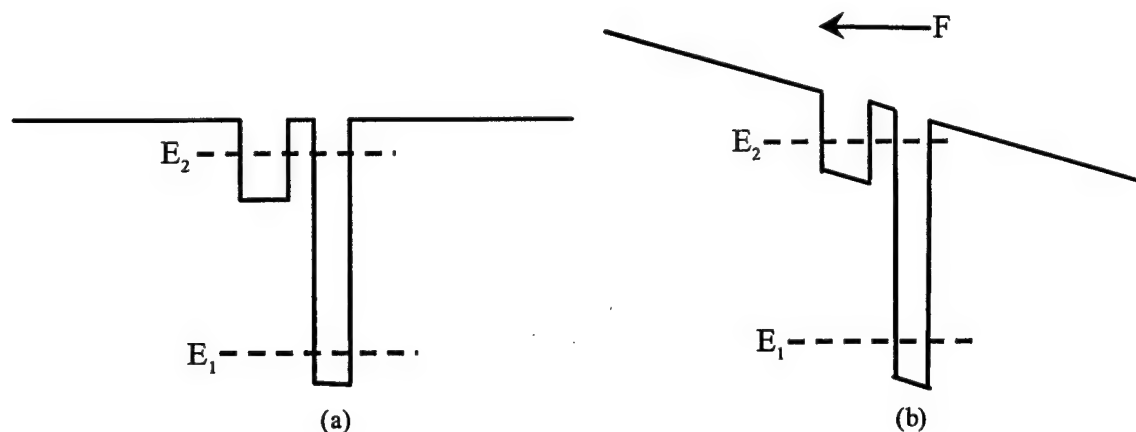


Figure 2.1 Schematic energy band diagrams of the asymmetric weakly coupled double quantum wells at (a) zero bias and (b) negative bias.

In the above structure, the left well is made of 70 Å undoped $\text{Al}_{0.2}\text{Ga}_{0.8}\text{As}$, the right well is made of 50 Å GaAs with doping density of $0.7 \times 10^{18} \text{ cm}^{-3}$, the two wells are separated by a 30 Å undoped $\text{Al}_{0.3}\text{Ga}_{0.7}\text{As}$, then a thick (400 Å) $\text{Al}_{0.3}\text{Ga}_{0.7}\text{As}$ is used as barrier to confine the two wells. The whole structure is repeated ten times and a top and bottom contacts (made of highly doped GaAs) are grown to form a QWIP. The devices were processed, and the dark current and the photo- responsivity were measured.

2.1.2 The Dark Current

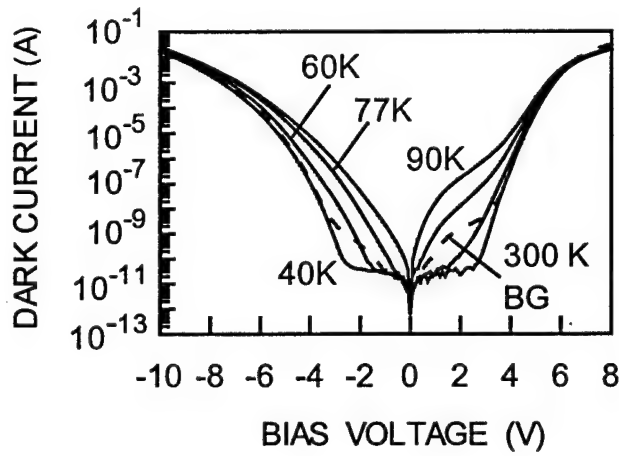


Figure 2.2 Dark current of Stark QWIP.

Figure 2.2 shows the dark current of the Stark QWIP. As can be seen from this figure, the device is under BLIP up to +3.5 V and -4.8 V at 40 K and -2 V and +3.0 V at 60 K. Here the BLIP means the dark current equals to the window current at a certain temperature.

2.1.3 The Responsivity

The responsivity of the Stark QWIP has been measured at 40 K and 77 K, the results are shown in figure 2.3 and figure 2.4, respectively. It is seen from figure 2.3 and 2.4 that the responsivity of this device are quite small at both 40 K and 77 K (the

responsivity increases a little bit at 77 K compared to that at 40 K). The peak wavelength is centered at 8 μm under different biases, and no obvious Stark shift was observed.

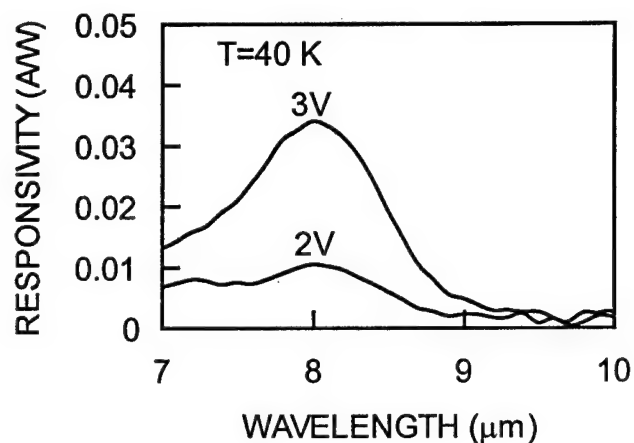


Figure 2.3 Responsivity of the Stark QWIP at 40 K.

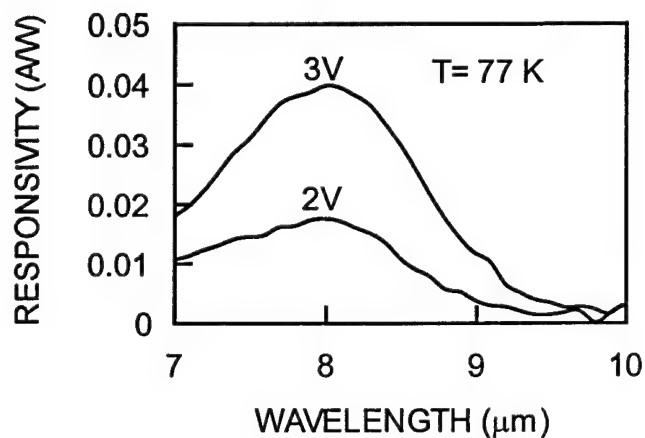


Figure 2.4 Responsivity of the Stark QWIP at 77 K.

2.1.4 Discussions

As stated above, the device does not show obvious Stark effect as we expected, the possible reason is due to the growth of wafer. We have processed the wafer for several times and the room temperature resistances for the devices are all very high, as can be seen from table 2.1.

Table 2.1 Room temperature resistance for the Stark QWIP.

Processing time	Ohmic contact recipe	Resistance at RT (K Ω)
1	AuGe/Ag/Au	2.7-22
2	AuGe/Ag/Au	2.1-19
3	AuGe/Ag/Au	20-23
4	AuGe/Ag/Au	2.5-21

Normally we expect the room temperature resistance of a QWIP to be around 100-200 ohm. The RT resistances for the Stark QWIP are too high and it may indicate that the growth of the wafer needs to be further improved in order to further check the Stark effect in this QWIP.

2.2 Broadband QWIPs

2.2.1 The Device Structure

Broadband LWIR detectors are important for some space science and earth observation missions [1]. A broadband QWIP is usually designed by repeating an unit of several quantum wells with slightly different peak wavelengths. The bound to continuous (b-c) states transition usually has a larger bandwidth compared to the bound to bound (b-b) and bound to quasi-bound (b-qb) transitions, and it will be beneficial to use b-c transitions in the wells consisting of the unit of the broadband QWIP. Figure 2.5 shows the schematic band diagram of the broadband QWIP in our experiment.

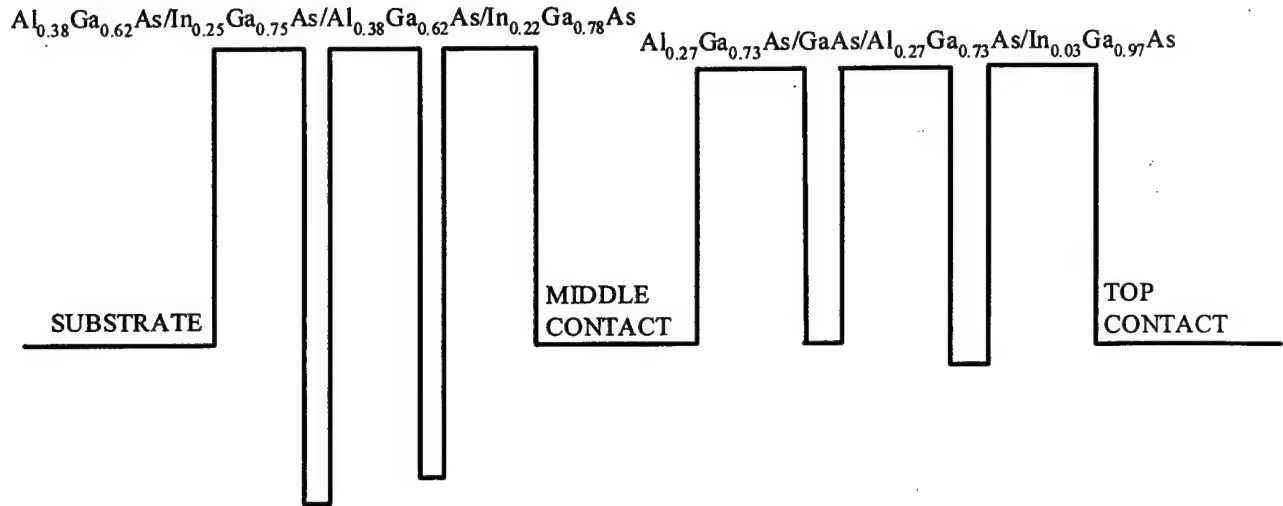


Figure 2.5 Schematic diagram of the broadband QWIP.

The broadband QWIP is a two- stack structure. The bottom stack consists of a well of 35 Å $\text{In}_{0.25}\text{Ga}_{0.75}\text{As}$ and another well of 35 Å $\text{In}_{0.22}\text{Ga}_{0.78}\text{As}$, the doping densities in both wells are $2.8 \times 10^{18} \text{ cm}^{-3}$. The two wells are separated by a barrier of 400 Å $\text{Al}_{0.38}\text{Ga}_{0.62}\text{As}$. The unit is then repeated for five times. The top stack consists of a well of 55 Å GaAs and a well of 55 Å $\text{In}_{0.03}\text{Ga}_{0.97}\text{As}$ with doping density of $0.5 \times 10^{18} \text{ cm}^{-3}$ in both wells, the barrier is made of 500 Å $\text{Al}_{0.27}\text{Ga}_{0.73}\text{As}$, and the whole unit is also repeated for five times. The top, middle and bottom contacts are made of highly doped GaAs (doping density $1 \times 10^{18} \text{ cm}^{-3}$).

2.2.2 The Dark Current

Figure 2.6 shows the dark current of the top stack. It is seen from this figure that the device is under BLIP up to +3.1 V and -3.3 V at 60 K.

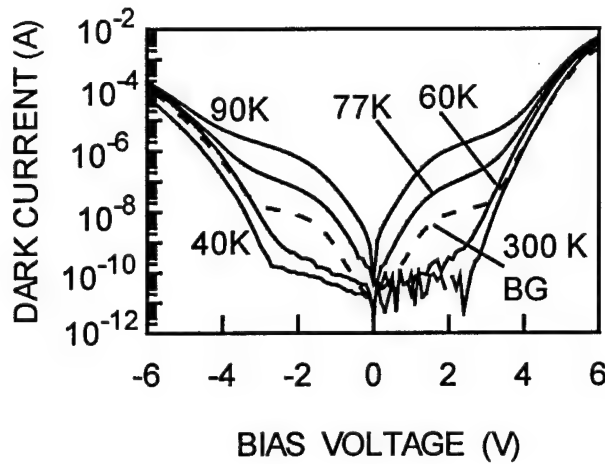


Figure 2.6 Dark current of the top stack.

2.2.3 The Responsivity

Figure 2.7 and 2.8 show the responsivity of the top stack under bias voltage of 2 V and 3 V at 40 K and 77 K, respectively. The peak wavelength is found to be at 8 μm . At 40 K and the bias voltage of 3 V, the cuton full width at half-maximum (FWHM) is at 7.45 μm and cutoff FWHM at 8.55 μm with a spectral width of 1.1 μm . At 40 K and 2V, the cuton FWHM is at 7.5 μm and cutoff FWHM is at 8.4 μm . At 77 K the spectral widths are almost the same as at 40 K.

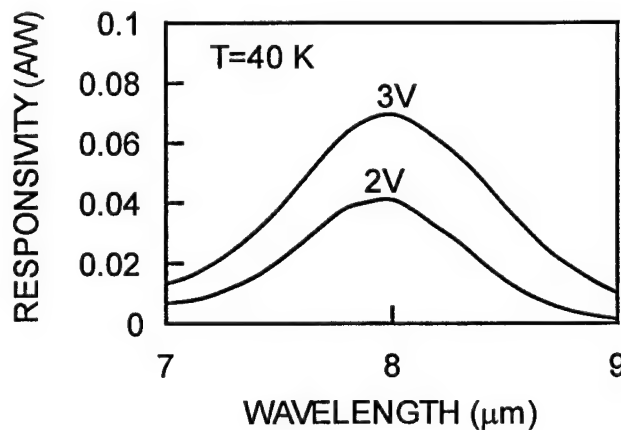


Figure 2.7 Responsivity of top stack at 40 K and bias voltages of 2 V and 3 V.

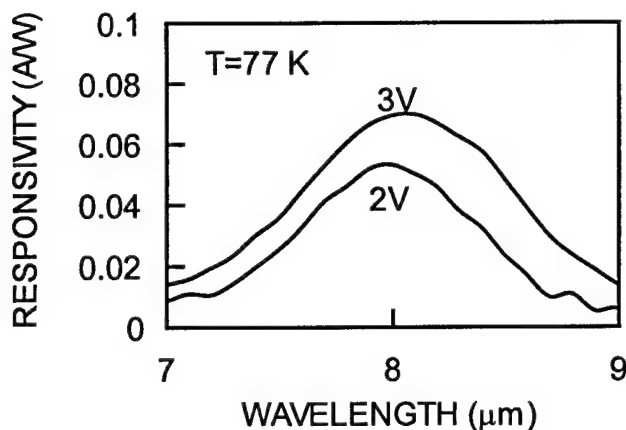


Figure 2.8 Responsivity of top stack at 77 K and bias voltages of 2 V and 3 V.

2.2.4 Discussions

From the responsivity shown previously, it is found the full width at half maximum (FWHM) of the top stack of this broadband QWIP is around 1 μm , which does not show a significant broadening of the response spectra. In the design only two different wells are used in an unit and the barrier width between the two wells are relatively too thick. Due to these reasons, we do not expect to see a very wide spectra. Also, the growth of the wafer is not perfect, the room temperature resistances for the devices are too large. Further work is being undertaken to further improve the performance of the two stack broadband QWIP.

2.3 Reference

1. S.V. Bandara, S.D. Gunapala, J.K. Liu, E.M. Luong, J.M. Mumolo, W. Hong, D.K. Sengupta and M.J. McKelvey, Appl. Phys. Lett. **72**, 2427 (1998).

3. Study of Intersubband Transition in Quantum Dots and Quantum Dot Infrared Photodetectors

3.1 Introduction

Studies of quantum dot structures have received considerable attention in recent years. It opens a new field in both fundamental physics and chemistry, and offers a wide range of potential applications for optoelectronic devices [1]. Quantum dots which form artificial atoms can be used to study many prominent effects such as Coulomb blockade, quantum Hall effect, and quantum chaos in such a structure [2,3]. Potential applications of quantum dots include semiconductor lasers [4,5], single electron transistors [6,7], quantum computing [8,9,10], optical memory [11], and cellular automata [12,13]. Several methods have been developed to grow quantum dot structures, including etching after growth of quantum wells [14,15], ion beam implantation and thermal annealing after growth of quantum wells [16], selective growth on patterned substrates [17,18] and the use of self-organization phenomena during epitaxial layer growth [19,20,21]. Fabrication of quantum dot structure using self-organization phenomena has received considerable attention in recent years due to its significant advantages over etching, ion beam implantation and selective growth techniques. The self-organized quantum dot structure has been successfully grown in both the III-V [22,23] and II-VI semiconductors [24] as well as in silicon and germanium systems [25,26].

Applications of quantum dot structures for long wavelength infrared (LWIR) detection in the 8-14 μm atmospheric spectral window have been reported recently [28-31]. Due to its unique structure and properties, a quantum dot infrared photodetector (QDIP) can absorb light incident from all directions without using grating couplers. The spectral response of a QDIP is usually very narrow due to the distribution of initial and final states. If the transition energies of the quantum dot levels are designed not to match

the longitudinal optical (LO) phonon energies, the recombination process via LO phonons can be suppressed, which will result in a longer excited electron lifetime and a higher signal-to-noise ratio. These unique properties could overcome some of the shortcomings encountered in the quantum well infrared photodetectors (QWIPs) [27]. Very little work has been reported on the study of QDIPs for LWIR detection [28,29]. Research in this area will not only improve our understandings of quantum confined structures but will also foster the development of new technologies in infrared lasers and detectors. In order to study the basic physics in quantum dots and developing QDIPs one must first study the intersubband transitions in quantum dots structures. Several experimental studies on the intersubband and interband transitions in quantum dots have been reported recently [29,30,31,32,33]. In addition, theoretical studies [34,35,36,37] on quantum dots have also been reported, primarily on the interband transitions. No theoretical work on intersubband transitions in quantum dots has been reported. In this paper we will use a method similar to that reported by Li *et al.* [37] to study the intersubband transitions in quantum dots and QDIPs for MWIR and LWIR detection.

3.2 Theoretical Consideration

In our calculation, the shape of a quantum dot is taken as a lens- like structure, which is considered as accurate in most cases of the quantum dot growth. The spatial distribution of quantum dots can be described as periodically arranged boxes [38]. Figure 3.1(a) and 3.1(b) show the schematic drawings of quantum dots along the growth direction (a) and in the growth plane (b), respectively. The in-plane and growth direction periods are denoted as L_{xy} and L_z , respectively. The vertical height of the dot is d , and the bottom diameter is $2R$, as shown in figure 3.1(a).

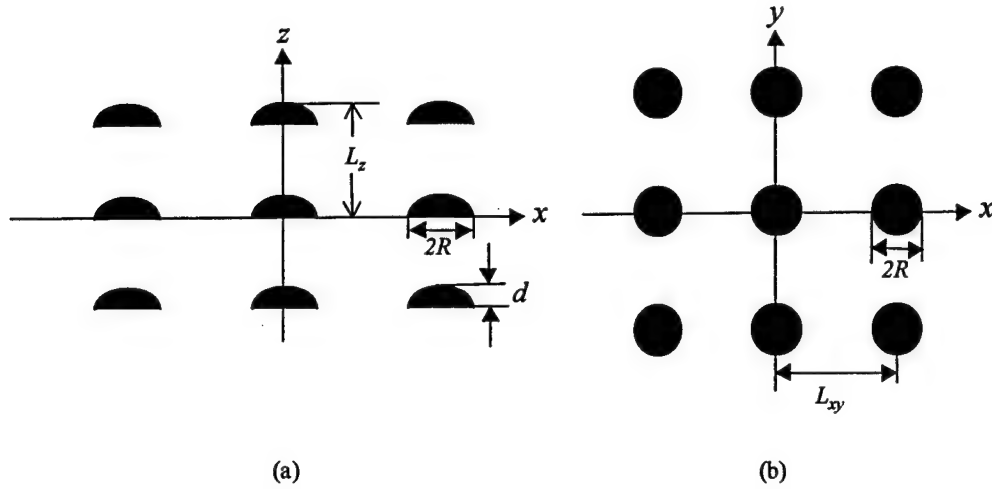


Figure 3.1 The schematic drawings of the distribution of quantum dots along the growth direction (a) and in the in-plane direction (b). The lens structure and dimensions of the quantum dot are also shown in (a); the diameter of the dot is $2R$, and the height is d .

The Schrödinger equation for electrons in the conduction band is given by

$$H\phi = E\phi, \quad (3.1)$$

where H , ϕ and E are the Hamiltonian, electron wave functions, and energy levels, respectively.

The Hamiltonian for the electrons can be written as

$$H = p \frac{1}{2m^*(x,y,z)} p + V(x,y,z), \quad (3.2)$$

where p is the electron momentum operator, and $m^*(x,y,z)$ is the electron effective mass (inside the dot it is denoted as m_d^* and m_b^* is in the barrier), and the potential experienced by the electrons can be expressed as

$$V(x,y,z) = \begin{cases} 0, & x^2 + y^2 \leq R^2, z \leq d \\ V_0, & \text{others.} \end{cases} \quad (3.3)$$

The electron wave functions are assumed to have the following form [35]

$$\phi = \frac{1}{L_{xy}\sqrt{L_z}} \sum_{n_x, n_y, n_z} C_{n_x, n_y, n_z} \exp\left\{i(k_{n_x}x + k_{n_y}y + k_{n_z}z)\right\}, \quad (3.4)$$

where $k_{nx}=k_x+n_xK_x$, $k_{ny}=k_y+n_yK_y$, $k_{nz}=k_z+n_zK_z$, $K_x=K_y=2\pi/L_{xy}$, $K_z=2\pi/L_z$, $n_x, n_y, n_z=0, \pm1, \pm2, \pm3, \text{ etc.}$ Substituting Eq. (3.4) into Eq. (3.1), one can obtain the following secular equation

$$\det \left[\begin{pmatrix} \frac{\hbar^2}{2m_b} \delta_{n_x, n_x'} \delta_{n_y, n_y'} \delta_{n_z, n_z'} + \frac{\hbar^2}{2m_{db}} S_1 S_2 \left(k_{n_x} k_{n_x'} + k_{n_y} k_{n_y'} + k_{n_z} k_{n_z'} \right) + \right. \\ \left. \left(\delta_{n_x, n_x'} \delta_{n_y, n_y'} \delta_{n_z, n_z'} - S_1 S_2 \right) V_0 - E \delta_{n_x, n_x'} \delta_{n_y, n_y'} \delta_{n_z, n_z'} \right] = 0, \quad (3.5)$$

where

$$k'_{nx}=k_x+n'_xK_x, k'_{ny}=k_y+n'_yK_y, k'_{nz}=k_z+n'_zK_z, \quad (3.6)$$

$$\frac{1}{m_{db}} = \frac{1}{m_d} - \frac{1}{m_b}, \quad (3.7)$$

$$S_1 = \begin{cases} \frac{d}{L_z}, & n_z = n'_z \\ \frac{\sin(\pi(n_z - n'_z)d/L_z)}{\pi(n_z - n'_z)}, & n_z \neq n'_z \end{cases} \quad (3.8a)$$

$$S_2 = \begin{cases} \frac{\pi R^2}{L_{xy}^2}, & n_x = n'_x, n_y = n'_y \\ \frac{R}{L_{xy} \sqrt{(n_x - n'_x)^2 + (n_y - n'_y)^2}} J_1 \left(\sqrt{(n_x - n'_x)^2 + (n_y - n'_y)^2} K_x R \right), & n_x \neq n'_x, \text{ or } n_y \neq n'_y \end{cases} \quad (3.8b)$$

Note that J_1 is the first-order Bessel function. By solving Eq. (3.5), we can obtain the energy levels and wave functions for the quantum dots. In our calculations the influence of strain effect on the band gap of dot material $\text{In}_x\text{Ga}_{1-x}\text{As}$ has been taken into account, i.e., $E_g = E_{g,0} + \Delta E_{g,s}$; $E_{g,0}$ is the band gap of $\text{In}_x\text{Ga}_{1-x}\text{As}$ without strain, and $\Delta E_{g,s}$ is the band gap variation caused by strain effect. For strain tensors, we assume $\epsilon_{xx} = \epsilon_{yy} = (a_0 - a)/a$,

where a_0 and a are the dot material and substrate (GaAs) lattice constants, respectively. ϵ_{ij} 's with $i \neq j$ are assumed to be 0, and ϵ_{zz} can be obtained by using $\epsilon_{zz} = -2(C_{12}/C_{11})\epsilon_{xx}$; C_{ij} 's are the elastic moduli of dot material. After treating strain in this way, $\Delta E_{g,s}$ can be written as $\Delta E_{g,s} = \Delta E_{g,c} + \Delta E_{g,H} + \Delta E_{g,U}$, where $\Delta E_{g,c}$, $\Delta E_{g,H}$ and $\Delta E_{g,U}$ are the rigid shift of conduction band, rigid shift of the valence band and shear uniaxial component, respectively [39]. The band offset parameter $Q_c = \Delta E_c / \Delta E_g$ is taken as 0.6, where ΔE_c and ΔE_g denote the conduction band offset and the energy gap difference between the dot and the barrier, respectively.

Having obtained the energy levels and wave functions, one can calculate the oscillator strength for the intersubband transition, i.e.,

$$f = \frac{2}{m} \frac{|\langle f | e \cdot p | i \rangle|^2}{E_f - E_i}, \quad (3.9)$$

where m is the electron mass, E_i and E_f are the energies of initial and final states, respectively. $|i\rangle$ and $|f\rangle$ are their respective wave functions. e is the unit vector in the direction of electric field.

3.3 Results and Discussion

We have performed calculations for two systems: one is the $\text{In}_x\text{Ga}_{1-x}\text{As}/\text{GaAs}$ material, and another is the $\text{InAs}/\text{Al}_x\text{Ga}_{1-x}\text{As}$ material. We first investigate the variation of the peak wavelengths and oscillator strengths with indium composition in the dot. The parameters used in our calculations are $L_x = L_y = 200 \text{ \AA}$, $L_z = 80 \text{ \AA}$, $d = 30 \text{ \AA}$, and $R = 50 \text{ \AA}$, at $k_x = k_y = k_z = 0$. In these two systems, we found that one bound state exists inside the quantum dot. The transition peak wavelengths for the $\text{In}_x\text{Ga}_{1-x}\text{As}/\text{GaAs}$ system are shown in figure 3.2. As shown in figure 3.2, when the indium composition x in the $\text{In}_x\text{Ga}_{1-x}\text{As}$ is

changed from 0.3 to 1, the peak wavelength for the bound ground state to first excited state transitions shifts from 20.7 μm to 13.2 μm , whereas the peak wavelength for the bound ground state to second excited state transitions changes from 10.4 μm to 7.6 μm . Thus, the $\text{In}_x\text{Ga}_{1-x}\text{As}/\text{GaAs}$ quantum dot system can be used for LWIR detection.

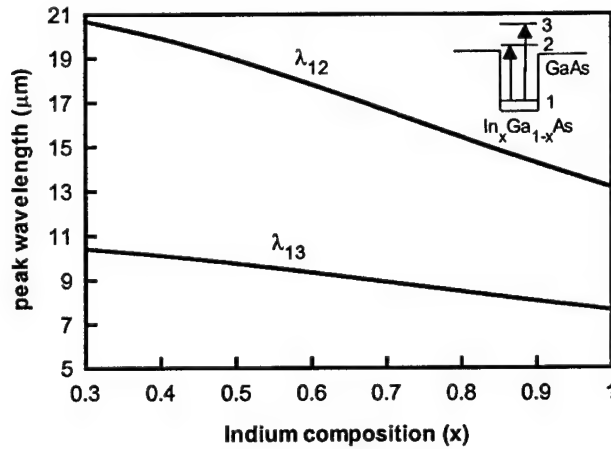


Figure 3.2 The intersubband transition peak wavelength versus indium composition x in an $\text{In}_x\text{Ga}_{1-x}\text{As}/\text{GaAs}$ quantum dot system. The inset shows the schematic energy band diagram and the intersubband transitions of this quantum dot.

Figure 3.3 shows the calculated oscillator strengths at $k_x=k_y=k_z=0$ for the transitions in the $\text{In}_x\text{Ga}_{1-x}\text{As}/\text{GaAs}$ quantum dot system. As can be seen from this figure, the transitions are highly polarized (i.e., transition in the growth direction is much larger than that of the in-plane transition). It can be shown that the ground state to the first excited states z -polarized transition has the largest oscillator strength.

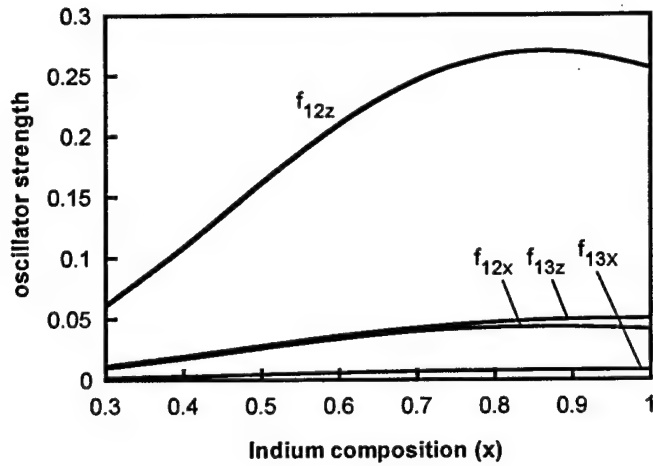


Figure 3.3 The calculated oscillator strength of the intersubband transitions in the $\text{In}_x\text{Ga}_{1-x}\text{As}/\text{GaAs}$ quantum dot system.

The calculated results for the $\text{InAs}/\text{Al}_x\text{Ga}_{1-x}\text{As}$ system are shown in figure 3.4. As the composition of aluminum (x) in the $\text{InAs}/\text{Al}_x\text{Ga}_{1-x}\text{As}$ system varies from 0 to 1, the peak detection wavelength for the bound to first excited state transitions shifts from $13.2\ \mu\text{m}$ to $4.7\ \mu\text{m}$, while the peak detection wavelength for the bound to second excited state transitions changes from $7.6\ \mu\text{m}$ to $3.3\ \mu\text{m}$. Thus, this QDIP system can be used for both the LWIR and MWIR detection.

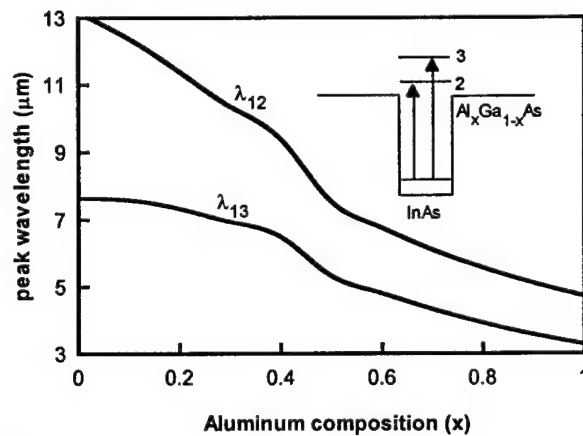


Figure 3.4 The intersubband transition peak wavelength versus aluminum composition x in an $\text{InAs}/\text{Al}_x\text{Ga}_{1-x}\text{As}$ quantum dot system. The inset shows the schematic energy band diagram and the intersubband transitions.

Figure 3.5 shows the oscillator strength associated with the intersubband transitions in the InAs/Al_xGa_{1-x}As quantum dot system at $k_x=k_y=k_z=0$. Similar to the case of In_xGa_{1-x}As/GaAs quantum dot system, the predominant transition is due to the ground to the first excited states z-polarized transition.

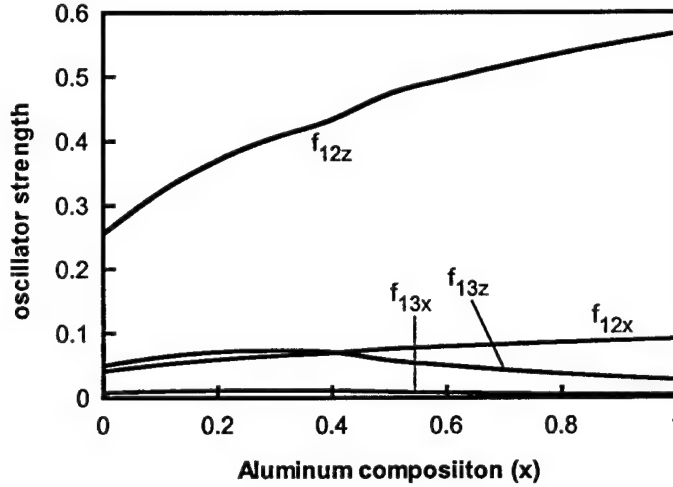


Figure 3.5 The calculated oscillator strength of the intersubband transitions in the InAs/Al_xGa_{1-x}As quantum dot system.

We next investigate the effect of quantum dot height and radius on the transition peak wavelengths and oscillator strengths in the InAs/GaAs and InAs/AlAs material systems. The results for InAs/GaAs system are shown in figure 3.6. Figure 3.6 (a) and (b) show the variation of peak wavelengths of transitions from the ground state to the first excited state and second excited state, respectively. Figure 3.6 (c) and (d) show the in-plane and growth-direction polarized oscillator strengths of the transition from the ground state to the first excited state, respectively. Figure 3.6 (e) and (f) show the in-plane and growth-direction polarized oscillator strengths of the transition from the ground state to the second excited state, respectively. It is seen from figure 3.6 (a) and (b) that both transition peak wavelengths decrease with increasing dot radius and height. This is due to the fact that increasing the dot radius and height, the energies of the ground state and excited states will decrease (with the energy of the ground state decreasing faster), which

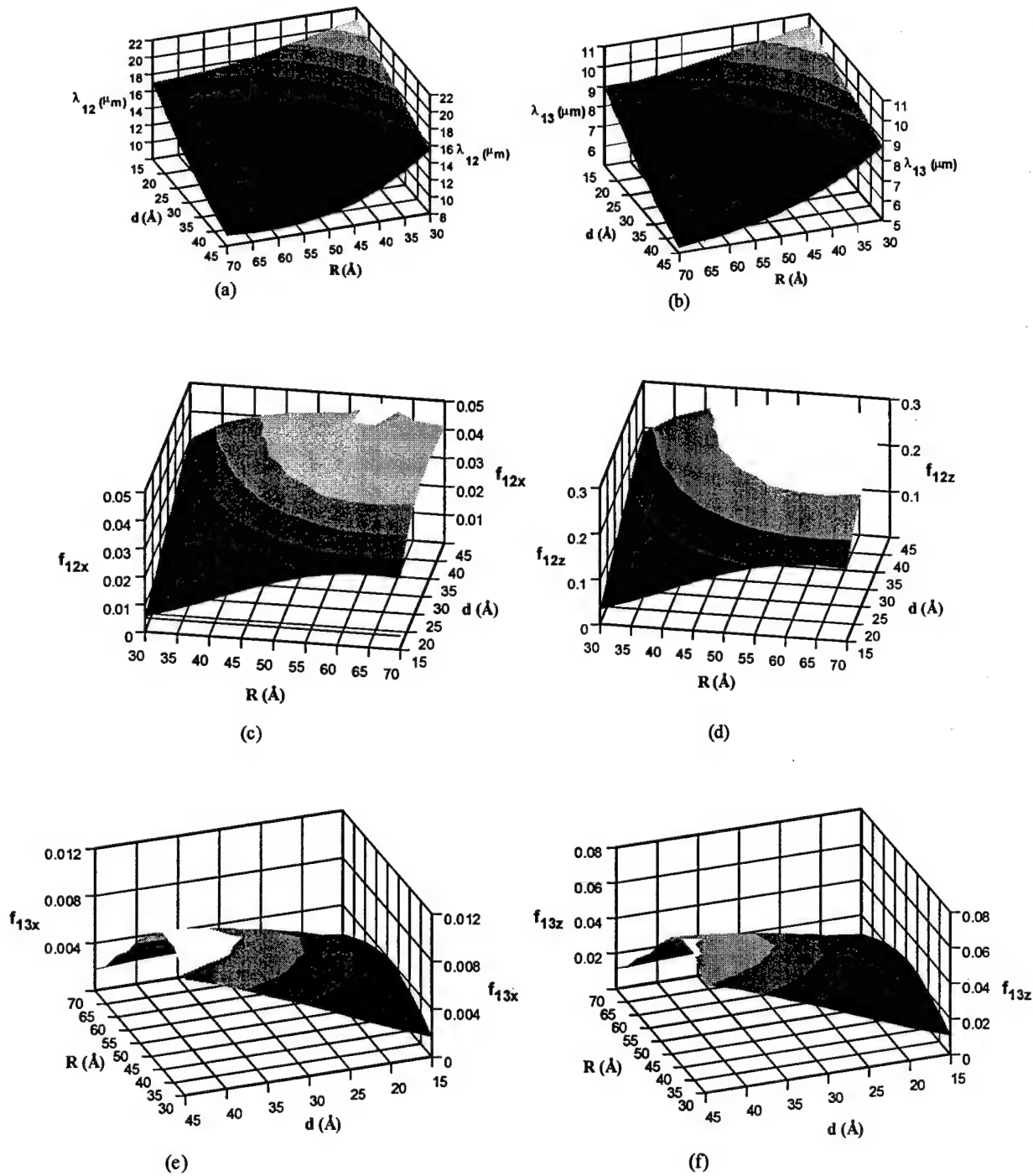


Figure 3.6 Variation of (a) λ_{12} , (b) λ_{13} , (c) f_{12x} , (d) f_{12z} , (e) f_{13x} and (f) f_{13z} with the height and radius of the quantum dot for the InAs/GaAs system. λ_{12} and λ_{13} are the peak wavelengths of transitions from the ground state to the first and second excited states, respectively; f_{12x} and f_{12z} are the in-plane and growth-direction polarized oscillator strengths of the transition from the ground state to the first excited state, respectively; f_{13x} and f_{13z} are the in-plane and growth-direction polarized oscillator strengths of the transition from the ground state

will result in a decrease of peak detection wavelength. As for the oscillator strengths, it was found from figure 3.6 (c)-(f) that the growth- direction polarized ground state to the first excited state transition is dominated over the entire range. There are two competing factors that determine the oscillator strength, one is the variation of energy difference between the initial and final states and another one is the overlapping of the wave functions of the two states. In the transition from the ground state to the first excited state, increasing the dot radius and height will lead to the increase of wave functions overlapping, which will result in an increase of oscillator strength. In the transition from the ground state to the second excited state, the wave functions overlapping dominates at first, when the dot radius and height continue to increase, the influence of energy difference will become dominant and the oscillator strength will decrease. As a result, we will see a saddle-like surface, as clearly shown in figure 3.6 (e) and (f).to the second excited state, respectively.

The results for the InAs/AlAs system are shown in figure 3.7. Figure 3.7 (a) through (f) have the similar meanings as figure 3.6 (a)-(f). The variation of transition peak wavelengths in the InAs/AlAs system is more complicated than the InAs/GaAs system. In the InAs/AlAs system, the peak wavelength of transitions from the ground to the second excited state decreases with increasing dot radius and height, which is similar to the case of InAs/GaAs system. However, the peak wavelength of transition from the ground to the first excited states decreases initially with the increase of dot radius and height, and then increases with dot radius after a certain value. This is due to fact that increasing the dot radius beyond a certain value the first excited state will also become a bound state and will decrease faster than the ground state energy, which will result in an increase of the peak wavelength. Also, the dominant transition is the growth-direction polarized ground state to the first excited state transition. For a fixed dot radius, the

oscillator strengths will decrease with increasing dot height; this is due to the fact that the influence of increasing energy difference exceeds that of the wave functions overlapping. On the other hand, for a fixed dot height, f_{13x} and f_{13z} decrease continually with the increasing dot radius, while f_{12x} and f_{12z} first increase and then decrease. This is due to the fact that for transition from the ground state to the second excited state, the influence of

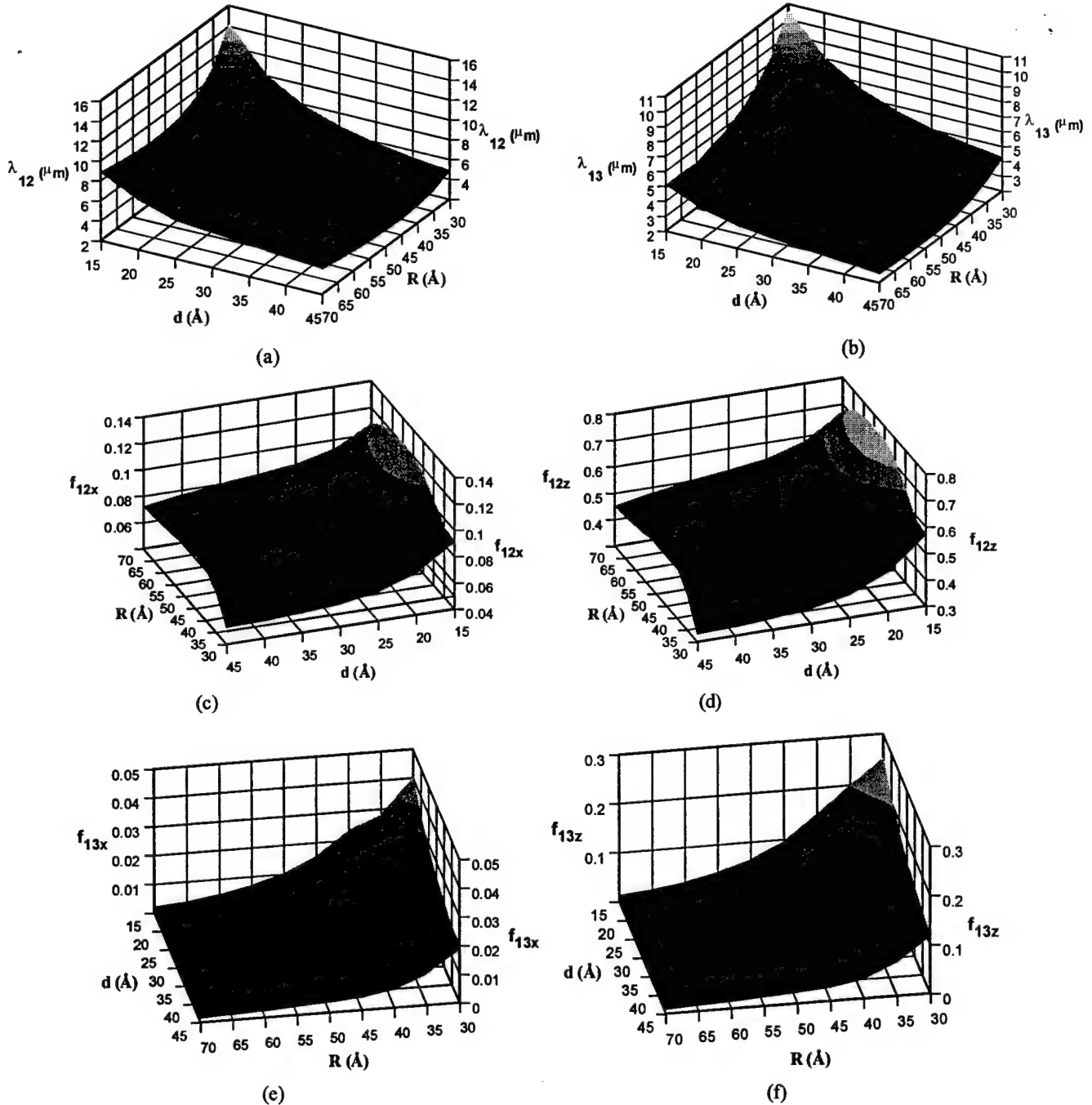


Figure 3.7 Variation of (a) λ_{12} , (b) λ_{13} , (c) f_{12x} , (d) f_{12z} , (e) f_{13x} and (f) f_{13z} with the height and radius of the quantum dot for an InAs/AlAs system.

increased transition energy is dominant all the time, while in the transition from the ground state to the first excited state, a more complicated competition exists between the variation of transition energy and the wave functions overlapping.

We next compare our calculated results with the published experimental data on the intersubband transitions in QDIPs. These QDIPs were all grown by using the self-organization phenomena during the epitaxial layer growth. During the growth, the dot size cannot be precisely controlled and the indium composition incorporated into the quantum dot is not exactly known, which makes detailed comparisons between the theory and the experiment rather difficult. In addition, we have used a "muffin-tin" potential to approximate the potential felt by an electron in the dot, and the influence of strain was taken into account by considering its effect on the energy band gap of the dot material, as discussed earlier. This approximation is good when R is large. However, if R is very small, then a more sophisticated model may be needed. Since recent experiments have revealed that the radius of the dot is quite large, we expect that this model should work well for the QDIPs under consideration. Besides, the average size and nominate indium composition are known, we expect the actual indium concentration in the dot is not far way from the nominate value. Based on these considerations we can make some semi-quantitative comparison and shed some light on the experimental results. In reference [29], the spectral response of a QDIP was measured, and two detection peaks were found in their device, one at $14.6\text{ }\mu\text{m}$ and another at $6.7\text{ }\mu\text{m}$. In the experiment both the growth and the in-plane direction transitions were observed. In our calculations, as can be seen from figure 2 that for $d=30\text{ }\text{\AA}$, and $R=50\text{ }\text{\AA}$ the calculated peak wavelengths for the ground to the first and second excited states transitions in an InAs/GaAs quantum dot structure are $13.2\text{ }\mu\text{m}$ and $7.6\text{ }\mu\text{m}$, respectively, which are in good agreement with the

observed peak wavelengths reported in reference [29]. In the experiment the absorption spectrum was not measured, but from their photoresponse measurements it shows that the z-polarized photoresponse of the 6.7 μm peak is much larger than the corresponding x-polarized photoresponse, in agreement with our calculated results that the growth-direction polarized transition is much stronger than the corresponding in-plane polarized transition. Pan *et al.* [30] reported an InGaAs/GaAs QDIP with intersubband transition peak wavelength at 13-14 μm under 45° facet incidence and at 14-15 μm under normal incidence illumination. Their results revealed that the absorption peak under 45° incidence is about seven times of that under normal incidence illumination. In our calculations for $d=30 \text{ \AA}$, and $R=50 \text{ \AA}$, in InAs/GaAs dot the transition peak from the ground state to first excited state is 13.2 μm , and the oscillator strength of the z-polarized transition is 6.2 times of the x-polarized transition. It can be seen from this result that our calculation agrees well with the experimental results given in reference [30] if we interpolate their results as originating from an InAs/GaAs dot system. In reference [31], several different forms of InAs/AlAs quantum dots were stacked together and intersubband peak wavelengths at 2.8, 3.2, 3.9 μm were observed from the photoconductivity spectrum. From figure 3.7(e) and (f) one can see that within a certain range of R and d , the transition peaks fall in the range of 2.5 μm to 5 μm , which are in line with the observed peak wavelengths.

Our calculations further reveal that the normal incident absorption is several times smaller than the growth-direction polarized absorption. In order to obtain optimal performance of QDIP under normal incident illumination, a grating coupler might still be needed. Our calculations also provide good guidance for the selection of dot parameters to obtain relatively large normal incident absorption in the QDIPs.

3.4 Conclusions

Theoretical studies on intersubband transitions in two quantum dot systems have been carried out in this work. The results show that for a typical dot size (dot radius of 50 Å and height of 30 Å), the intersubband transitions in the $\text{In}_x\text{Ga}_{1-x}\text{As}/\text{GaAs}$ quantum dot system cover the 7-13 μm LWIR and 13-20 μm VLWIR spectral ranges as x varies from 0.3 to 1. The intersubband transitions in an $\text{InAs}/\text{Al}_x\text{Ga}_{1-x}\text{As}$ quantum dot system can cover both the LWIR and MWIR (13 - 4 μm) regions with x varying from 0 to 1. Calculations of the transition peak wavelengths and oscillator strengths as a function of the dot size in InAs/GaAs and InAs/AlAs systems have been carried out in this work. The calculated intersubband transition peak wavelengths and oscillator strengths are in good agreement with the published data [29-31]. The calculations performed here provide a good guidance for the design of QDIPs for both MWIR and LWIR applications and a better understanding of the intersubband transition phenomena in quantum dots.

3.5 References

1. M.A. Reed, Scientific American 268 (1993) 118.
2. R.C. Ashoori, Nature 379 (1996) 413.
3. L. Kouwenhoven, C. Marcus, Physics World 11 (1998) 35.
4. N. Kristaedter, O.G. Schmidt, N.N. Ledentsov, D. Bimberg, V.M. Ustinov, A.Y. Egorov, M.V. Maximov, P.S. Kop'ev, Zh. I. Alferov, Appl. Phys. Lett. 69 (1996) 1226.
5. D. Bimberg, N.N. Ledentsov, M. Grundmann, F. Heinrichsdorff, V.M. Ustinov, P.S. Kop'ev, Zh.I. Alferov, J.A. Lott, Solid-State Electronics 42 (1998) 1433.

6. E. Leobandung, L. Guo, S.Y. Chou, *Appl. Phys. Lett.* 67 (1995) 2338.
7. L. Guo, E. Leobandung, S.Y. Chou, *Science* 275 (1997) 649.
8. K.K. Likharev, *IBM J. Res. Dev.* 32 (1988) 1444.
9. P.D. Tougaw, C.S. Lent, *J. Appl. Phys.* 75 (1994) 1818.
10. D. Loss, D.P. DiVincenzo, *Phys. Rev. A* 57 (1998) 120.
11. K. Imamura, Y. Sugiyama, Y. Nakata, S. Muto, N. Yokoyama, *Jpn. J. Appl. Phys.* 34 (1995) L1445.
12. C.S. Lent, P.D. Tougaw, W. Porod, G.H. Bernstein, *Nanotechnology* 4 (1993) 49.
13. G.L. Snider, A.O. Orlov, I. Amlani, G.H. Bernstein, C.S. Lent, J.L. Merz, W. Porod, *Solid-State Electronics* 42 (1998) 1355.
14. P.M. Petroff, A.C. Gossard, R.A. Logan, W. Wiegmann, *Appl. Phys. Letts.* 41 (1982) 635.
15. Y. Miyamoto, M. Cao, Y. Shingai, K. Furuya, Y. Suematsu, K.G. Ravikumar, S. Arai, *Jpn. J. Appl. Phys.* 26 (1987) L225.
16. Y. Hirayama, Y. Suzuki, S. Tarucha, H. Okamoto, *Jpn. J. Appl. Phys.* 24 (1985) L516.
17. T. Fukui, S. Ando, *Electron. Lett.* 25 (1989) 410.
18. E. Kapon, D.M. Hwang, R. Bhat, *Phys. Rev. Lett.* 63 (1989) 430.
19. D. Leonard, M. Krishnamurthy, C.M. Reaves, S.P. Denbaars, P.M. Petroff, *Appl. Phys. Lett.* 63 (1993) 3203.
20. S. Hara, J. Motohisa, T. Fukui, H. Hasegawa, *Jpn. J. Appl. Phys.* 34 (1995) 4401.
21. P. J. Pearah, A.C. Chen, A.M. Moy, K.C. Hsieh, K.Y. Cheng, *IEEE J. Quantum Electron.* QE-30 (1994) 608.
22. A.C. Gossard, S. Fafard, *Solid State Communications* 92 (1994) 63.
23. P. M. Petroff, S.P. DenBaars, *Superlattices and Microstructures* 15 (1994) 15.

24. J.L. Merz, S. Lee, J.K. Furdyna, *J. Cryst. Growth* 184/185 (1998) 228.
25. A. Fissel, K. Pfennighaus, W. Richter, *Thin Solid Films* 318 (1998) 88.
26. P. Schittenhelm, C. Engel, F. Findeis, G. Abstreiter, A.A. Darhuber, G. Bauer,
A.O. Kosogov, P. Werner, *J. Vac. Sci. Technol. B* 16 (1998) 1575.
27. B.F. Levine, *J. Appl. Phys.* 74 (1993) R1.
28. S. Kim, H. Mohseni, M. Erdtmann, E. Michel, C. Jelen, M. Razeghi, *Appl. Phys.*
Lett. 73 (1998) 963.
29. S. Maimon, E. Finkman, G. Bahir, S.E. Schacham, J.M. Garcia, P.M. Petroff,
Appl. Phys. Lett. 73 (1998) 2003.
30. D. Pan, Y.P. Zeng, M.Y. Kong, J. Wu, Y.Q. Zhu, C.H. Zhang, J.M. Li, C.Y.
Wang, *Electronics Letters* 32 (1996) 1726.
31. K. W. Berryman, S.A. Lyon, Mordechai Segev, *Appl. Phys. Lett.* 70 (1997) 1861.
32. R.J. Warburton, C.S. Dür, K. Karrai, J.P. Kotthaus, G. Medeiros-Ribeiro and P.M.
Petroff, *Phys. Rev. Lett.* 79 (1997) 5282.
33. C.S. Dür, R.J. Warburton, K. Karrai, J.P. Kotthaus, G. Medeiros-Ribeiro and P.M.
Petroff, *Physica E* 2 (1998) 23.
34. Lin-Wang Wang, A. Zunger, *Journal of Physical Chemistry* 98 (1994) 2158.
35. J.-Y. Marzin, G. Bastard, *Solid State Communications* 92 (1994) 437.
36. M. Grundmann, O. Stier, D. Bimberg, *Phys. Rev. B* 52 (1995) 11969.
37. Shu-Shen Li, Jian-Bai Xia, Z.L. Yuan, Z. Y. Xu, Weikun Ge, Xiang Rong Wang, Y.
Wang, J. Wang, L.L. Chang, *Phys. Rev. B* 54 (1996) 11575.
38. Qianghua Xie, Anupan. Madhukar, Ping Chen, Nobuhiko P. Kobayashi, *Phys. Rev.*
Lett. 75 (1995) 2542.
39. M. Sugawara, N. Okazaki, T. Fujii and S. Yamazaki, *Phys. Rev. B* 48 (1993) 8102.

4. Very-Long-Wavelength Quantum Well Infrared Photodetectors

4.1 Introduction

Intersubband transitions in III-V semiconductor heterostructures have been widely investigated for quantum well infrared photodetectors (QWIPs) applications [1]. Due to its material growth maturity, large array uniformity and detection wavelength flexibility, high performance and large format (640×480) GaAs/AlGaAs QWIP focal plane arrays (FPAs) have been successfully demonstrated, which challenge other infrared detector systems such as HgCdTe, PtSi, InSb, and Si:Ge for the mid-wavelength infrared (MWIR) and long-wavelength infrared (LWIR) detection. Most of the QWIP research works have been focused on the spectral regions of MWIR (3-5 μm) and LWIR (8-12 μm) bands during the past decade. Various QWIP structures have been developed to meet different application requirements. In addition, several light-coupling and grating techniques have been developed to increase the absorption quantum efficiency of QWIPs in the mid- and long- wavelength infrared atmospheric spectral windows [2, 3].

In this paper, we will emphasize on the very long wavelength IR (VLWIR) detectors. The VLWIR detectors are of great interest for many applications such as measuring vertical temperature profiles of the atmosphere, studying the composition, structure, and the energy balance of molecular clouds and stars. It is especially important in strategic and space applications to detect far away targets with a cold background. These applications have placed stringent requirements on the performance of IR detectors and arrays such as high detectivity, low dark current, high uniformity, radiation hardness, and low power dissipation. The current state of the art HgCdTe (MCT) based IR detectors have not met all these requirements, and QWIPs provide a useful alternative for VLWIR applications.

Recent works on the VLWIR QWIPs fabricated from GaAs/AlGaAs material systems have been reported by several researchers with peak detection wavelengths ranging from 15 μm to 26.9 μm [4,5,6,7,8,9]. Table I summarizes the key device parameters, peak detection wavelengths, and detectivity of these QWIPs.

Table I Main results of works on VLWIR QWIPs reported in the literature.

Ref	Well width	Barrier thickness	$N_D(\text{cm}^{-3})$	$\lambda_p(\mu\text{m})$	$D^*(\text{cm Hz}^{1/2}/\text{W})$
4	72 Å GaAs	600 Å $\text{Al}_{0.13}\text{Ga}_{0.87}\text{As}$	2.5×10^{17}	17.5	3×10^{12} (40 K)
	72 Å GaAs	600 Å $\text{Al}_{0.135}\text{Ga}_{0.865}\text{As}$	2.5×10^{17}	16.8	
	72 Å GaAs	600 Å $\text{Al}_{0.14}\text{Ga}_{0.86}\text{As}$	2.5×10^{17}	16.5	
	72 Å GaAs	600 Å $\text{Al}_{0.145}\text{Ga}_{0.855}\text{As}$	2.5×10^{17}	15.9	
	66 Å GaAs	600 Å $\text{Al}_{0.145}\text{Ga}_{0.855}\text{As}$	2.5×10^{17}	15.6	
	66 Å GaAs	600 Å $\text{Al}_{0.15}\text{Ga}_{0.85}\text{As}$	2.5×10^{17}	15.3	
	66 Å GaAs	600 Å $\text{Al}_{0.155}\text{Ga}_{0.845}\text{As}$	2.5×10^{17}	15.0	
5	70 Å GaAs	500 Å $\text{Al}_{0.1}\text{Ga}_{0.9}\text{As}$	3×10^{17}	16.6	2×10^{12} (20 K)
6	80 Å $\text{In}_{0.15}\text{Ga}_{0.85}\text{As}$	500 Å GaAs	5×10^{17}	15.3	8×10^9 (10 K)
	85 Å $\text{In}_{0.15}\text{Ga}_{0.85}\text{As}$	500 Å GaAs	1×10^{17}	17.8	9.7×10^{10} (10 K)
7	60 Å GaAs	500 Å $\text{Al}_{0.15}\text{Ga}_{0.85}\text{As}$	8×10^{17}	15	2×10^{11} (30 K)
8	118 Å GaAs	400 Å $\text{Al}_{0.07}\text{Ga}_{0.93}\text{As}$	1.5×10^{17}	26.9	2.5×10^9 (4.2 K)
9	p-type superlattice	p-type superlattice		19.2	2.58×10^7 (20 K)
	35 Å $\text{In}_{0.27}\text{Ga}_{0.73}\text{As}$	32 Å $\text{Al}_{0.15}\text{Ga}_{0.85}\text{As}$			

Major effort on VLWIR QWIP development has been made at Jet Propulsion Laboratory (JPL) for space applications. A 128×128 pixel QWIP FPA with a 15 μm cutoff wavelength has been demonstrated by JPL with an NEDT of 30 mK at 45 K with 300 K background and $f/2.3$ optics [10]. This initial array gives excellent images with a

99.9 % operability and a 2.4 % uncorrected responsivity nonuniformity. Comparing the array results from both the MCT detector and GaAs QWIP at 15 μm , QWIP has higher operability and uniformity due to the mature GaAs MBE growth and processing technology.

4.2 Design Consideration of VLWIR QWIPs

Several issues need to be considered when designing a VLWIR QWIP. In a VLWIR scenario, the temperature of the target is usually cold and the energy density of the blackbody radiation is small. This means that a higher response is needed from the detector. In order to tailor the peak detection wavelength of a QWIP to the VLWIR spectral region, the barrier height needs to be lowered and the well width needs to be increased with respect to MWIR (3-5 μm) and LWIR (8-12 μm) QWIPs. For QWIPs operating in the LWIR region, the typical well width is about 40 \AA to 45 \AA , and the aluminum mole fraction in the barrier is about 25% to 30%. While for VLWIR QWIPs, the well width is usually larger than 60 \AA , and the aluminum mole fraction in the barrier is less than 15% in order to achieve lower barrier energy and longer peak detection wavelength. The lower energy barrier and wider well width will result in a smaller activation energy, which means a higher thermionic emission of electrons from the quantum wells. In order to reduce the thermionic mission, which is the dominant mechanism of dark current in a VLWIR QWIP, the doping density in the well needs to be lower than that of a LWIR QWIP. In a LWIR QWIP, typical doping density is usually 0.5 to $1 \times 10^{18} \text{ cm}^{-3}$, whereas in a VLWIR QWIP the doping density is about 2 to $3 \times 10^{17} \text{ cm}^{-3}$. A balance between the responsivity and the dark current needs to be considered when choosing the doping density. The corresponding D^* will also be affected. In general, under the same operating temperature, the longer the detector cutoff wavelength, the smaller the D^* value. The electron density in the quantum well of a QWIP is usually

very high, and hence the exchange energy plays an important role in the intersubband transition energy. This is especially true for a VLWIR QWIP in which the exchange energy greatly affects the detection peak wavelength due to the low barrier energy. We shall discuss each of these effects in detail next.

4.2.1 Blackbody Radiation

The blackbody radiation spectral density decreases very rapidly when the target temperature decreases. Figure 4.1 shows the blackbody spectral density calculated under different temperatures using the blackbody spectral density formula

$$W(\lambda) = \frac{2\pi c^2 h}{\lambda^5} \frac{1}{\exp(hc/\lambda k_b T_B) - 1} \quad (4.1)$$

where c , h , k_b and T_B are the light speed in vacuum, Planck constant, Boltzmann constant, and the background temperature, respectively. As can be seen in Fig. 4.1, when the target temperature changes from 300 K to 200 K, the peak wavelength will shift from 10 μm to 15 μm , and the spectral density will also decrease. For example, the maximum spectral density at 200 K is only 13% of the maximum density at 300 K. In order to efficiently detect the radiation from a target at 200 K, a 15 μm detector with higher responsivity, or lower dark current is highly desirable to maintain the same sensitivity as a 10 μm detector for a 300 K target.

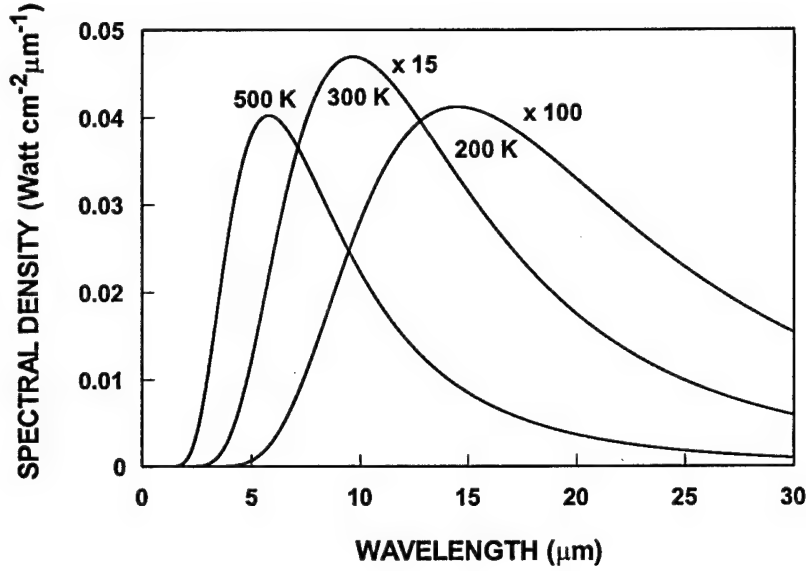


Figure 4.1 Blackbody spectral density at 200, 300, and 500 K.

4.2.2 Dark Current and Dynamic Resistance

The dark current I_d of a QWIP can be expressed as [11]

$$I_d = \frac{e m_w^* A}{\pi \hbar^2 L_p} \frac{\mu F}{\sqrt{1 + (\mu F / v_s)^2}} \int_{E_i}^{\infty} f(E) T(E, F) dE \quad (4.2)$$

where e is the electronic charge, m_w^* is the electron effective mass in the well, A is the device area, L_p is the QWIP period length, μ is the electron mobility, F is the electric field inside the QWIP, v_s is the electron saturation velocity, $f(E)$ is the Fermi-Dirac distribution function, and $T(E, F)$ is the bias-dependent tunneling current transmission coefficient for a single barrier. When the thermionic emission is dominant, the dark current can be expressed as

$$I_d = \frac{e^2 m_w^* A}{\pi \hbar^2} \frac{\mu F^2}{\sqrt{1 + (\mu F / v_s)^2}} \frac{L_b}{L_w} \exp \left\{ - \frac{(E_b - eF L_w - E_F - E_i)}{k_b T} \right\} \quad (4.3)$$

The dynamic impedance Z of a single period QWIP is defined as

$$Z = \frac{dV}{dI_d} \quad (4.4)$$

where V is the voltage drop across one period of the QWIP. In our calculations, the electron mobility and saturation velocity are taken as $2000 \text{ cm}^2 \cdot \text{V}^{-1} \cdot \text{s}^{-1}$ and $2 \times 10^6 \text{ cm/s}$, respectively. Figure 4.2 shows the calculated dark current versus bias for the $15.5 \text{ }\mu\text{m}$ and $9.2 \text{ }\mu\text{m}$ QWIPs at $T=40 \text{ K}$ and 60 K , respectively. The device structure for the $15.5 \text{ }\mu\text{m}$ QWIP uses a $66 \text{ }\text{\AA}$ GaAs well and a $600 \text{ }\text{\AA}$ $\text{Al}_{0.15}\text{Ga}_{0.85}\text{As}$ barrier with a doping density of $2.5 \times 10^{17} \text{ cm}^{-3}$. The device structure for the $9.2 \text{ }\mu\text{m}$ QWIP uses a $66 \text{ }\text{\AA}$ GaAs well with a doping density of $5 \times 10^{17} \text{ cm}^{-3}$ and a $600 \text{ }\text{\AA}$ $\text{Al}_{0.25}\text{Ga}_{0.75}\text{As}$ barrier. As can be seen from this figure, the dark current of the $9.2 \text{ }\mu\text{m}$ QWIP is several orders of magnitude lower than that of the VLWIR QWIP under same bias and temperature condition. As a result, a large difference in the dynamic resistance of these two detectors is expected, as shown in figure 4.3. Therefore, in order for the $15.5 \text{ }\mu\text{m}$ QWIP to have the same performance as the $9.2 \text{ }\mu\text{m}$ QWIP, a lower operating temperature is required.

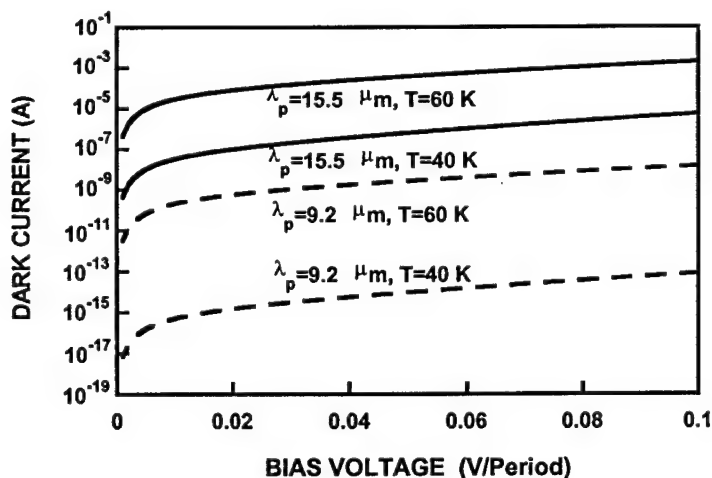


Figure 4.2 Calculated dark current versus bias for two QWIPs with peak wavelengths at $9.2 \text{ }\mu\text{m}$ and $15.5 \text{ }\mu\text{m}$, respectively.

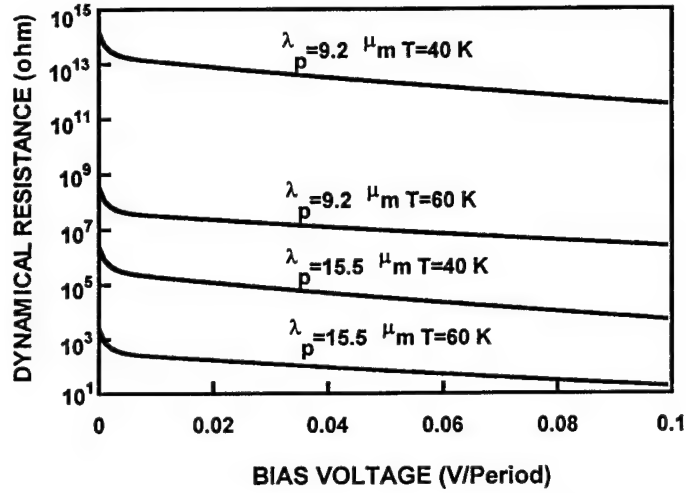


Figure 4.3 Calculated dynamic resistances for two QWIPs with peak wavelengths at 9.2 μm and 15.5 μm , respectively.

4.2.3 Detectivity

In a VLWIR QWIP the main dark current conduction mechanism is due to the thermionic emission across the barrier of quantum well. In general, over a wide range of temperatures and cutoff wavelengths, the detectivity can be expressed as [1]

$$D^* = D_0^* \exp(hc / 2 \lambda_c k_b T) \quad (4.5)$$

where λ_c is the cutoff wavelength.

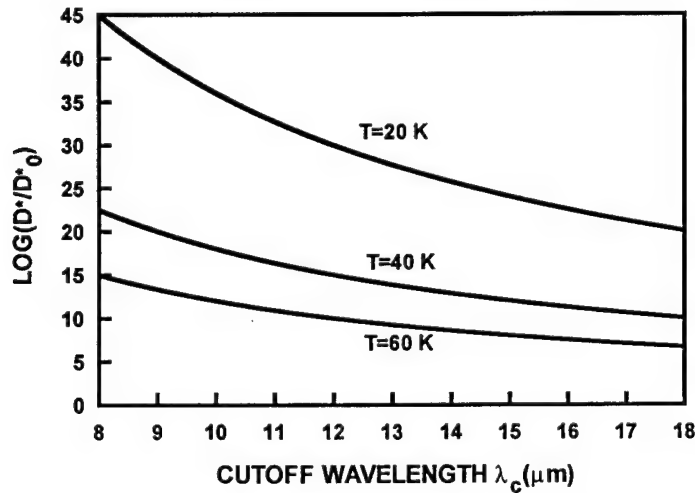


Figure 4.4 Variation of normalized detectivity with cutoff wavelength in the long and very long wavelength infrared (VLWIR) region.

As shown in figure 4.4, the detectivity decreases with increasing cutoff wavelength and temperature. This is due to the fact that with the increase of cutoff wavelength and temperature, the dark current and hence the dark current noise will increase significantly with increasing cutoff wavelength and temperature due to the nature of thermionic emission, while the responsivity remains unchanged over a wide range of temperatures. Therefore, we come to the conclusion that in order to keep the same D^* when extending to longer wavelength, a lower operating temperature is needed.

4.2.4 Peak Wavelength Shift due to Exchange Interaction

When designing a QWIP, the energy states are obtained from the Schrödinger equation by taking into account the potential at the heterojunction caused by the energy band offset of the quantum well and barrier materials. The peak detection wavelength of a VLWIR QWIP can be calculated by using the transfer matrix method (TMM) [12]. West [13] has calculated the Coulomb interaction (repulsive) of the electrons in the quantum well and found that it is very small, which is canceled out with the dynamic electron plasma interaction. However, the experimental data he observed was about 6 meV higher than the calculated value for several QWIP structures. Taking into account the exchange interaction, excellent agreement between the theory and the experiment can be obtained [14]. For a VLWIR QWIP, the transition energy is relatively small and the influence of exchange energy becomes very significant. The exchange energy can be expressed as [14]

$$E_{exch} = -\frac{e^2 k_f}{2\varepsilon} \int_0^{\frac{d^2 k'}{(2\pi)^2}} \int dz \int d z' \frac{e^{-|k-k'||z-z'|}}{|k-k'|} |\phi_1(z)|^2 |\phi_1(z')|^2 \quad (4.6)$$

where $k_f = (2\pi\sigma)^{1/2}$, σ is the two-dimensional electron density in the quantum well, ε is the dielectric constant, k and k' are the in-plane wave vectors of electrons. Under normal

doping condition, the exchange energy will lower the ground state subband energy by 5 to 10 meV and shifts the absorption peak to shorter wavelength.

As mentioned previously, in order to design a QWIP with peak detection wavelength in the VLWIR region, the barrier height should be lowered than that of the LWIR QWIP, and the well width should be increased with a lower doping density. As an example, let us consider the design of a VLWIR QWIP with a GaAs well width of L_w and doping density of $N_D = 2.5 \times 10^{17} \text{ cm}^{-3}$ and a 600 Å $\text{Al}_{0.15}\text{Ga}_{0.85}\text{As}$ barrier. Figure 4.5 shows the calculated variation of peak detection wavelength with well width L_w ; the dashed line is the result without considering the exchange energy, while the solid line is the result of taking into account the exchange energy. The result agrees well with the experiment (e.g., at $L_w=66 \text{ Å}$, the calculated peak wavelength is 15.54 μm and the measured value is 15.3 μm [4]). The reason for the transition peak wavelength to decrease with increasing well width is that: in this system the transition occurs between the bound state and the continuum state, and increasing well width has little effect on the excited continuum state energy but significantly decreases the bound state energy. As a result, the peak detection wavelength will decrease with the increase of well width and show a blue shift. As can be seen from this figure that the exchange energy plays an important role on the peak detection wavelength in a VLWIR QWIP. Therefore, special attention should be paid to the doping density while designing the VLWIR QWIP.

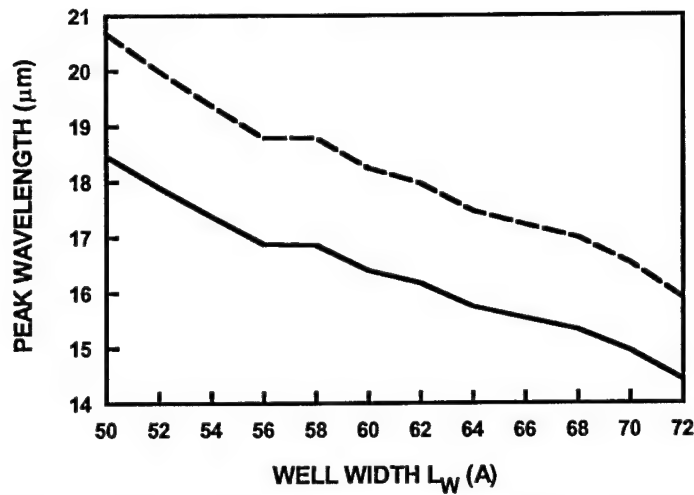


Figure 4.5 Variation of peak wavelength with well width in a GaAs/Al_{0.15}Ga_{0.85}As VLWIR QWIP. The dashed line is without considering the exchange energy, while the solid line is taking into account the exchange energy. L_w is the well width, and the barrier thickness is 600 Å.

4.3 VLWIR QWIP in a Multicolor QWIP Stack

As the infrared (IR) detector technology continues to advance, there is a growing demand for multi-color IR detectors for advanced sensing and imaging systems. IR detectors with more than two colors are highly desirable for temperature registration, chemical analysis, and target discrimination and identification. Using multiple stacks of QWIPs with intermediate contact layers, the capability of multicolor detection simultaneously, or sequentially by tuning the bias voltage has been demonstrated [15,16]. When a VLWIR stack is incorporated in a multi-color QWIP, special attention has to be paid in the design. As can be seen from figure 3, the dynamic resistance of the $\lambda_p=15.5$ μm QWIP is much smaller than that of the $\lambda_p=9.2$ μm QWIP under the same bias condition. This means that the dark current, and hence the operating temperature of a multi-stack, multi-color QWIP will be limited by the longer wavelength QWIP stack. If operating temperature is the primary requirement, reducing the VLWIR dark current should be the main consideration when designing the detector. A low dynamic resistance also means a low voltage drop on this stack. When the multi-stack QWIP is used under

voltage tunable mode, careful selection of period number, doping density and barrier width is necessary in order to realize the voltage tunability with a reasonable bias.

4.4 A 14.7 μm VLWIR QWIP

In this section we discuss the design, fabrication, characterization, and performance of a VLWIR QWIP. The QWIP structure is composed of 20 periods 80 Å $\text{In}_{0.04}\text{Ga}_{0.96}\text{As}$ well with doping density of $2 \times 10^{17} \text{ cm}^{-3}$ and a 500 Å $\text{Al}_{0.09}\text{Ga}_{0.91}\text{As}$ barrier. The schematic conduction band diagram of this QWIP is shown in figure 4.6. This structure is similar to those listed in table I with some unique features. First, a small amount of indium is added in the GaAs well region. This gives a smaller effective mass of electron, and therefore a higher absorption in the quantum well. Using aluminum free GaAs as a barrier has the advantage of having smaller defect center in the barrier which tends to reduce the dark current. However, electrons in the heavily doped GaAs contact layer can also tunnel into the quantum wells without any potential barrier, therefore causes an increase in dark current. In this design, a small amount of Al is added in the GaAs barrier to reduce the device dark current.

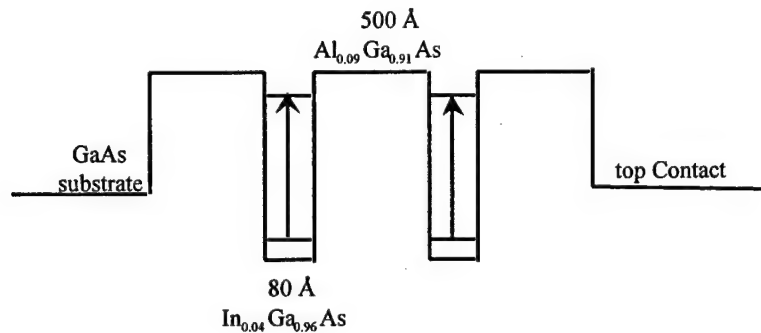


Figure 4.6 Schematic conduction band diagram of a 14.7 μm bound to bound state transition GaAs/AlGaAs QWIP.

The detector was designed with a peak wavelength at 14.5 μm . Theoretical calculation shows that the peak wavelength of this QWIP is at 16.1 μm without considering the exchange energy and 14.67 μm after taking into account the exchange energy. The detector is designed to use the bound to bound state intersubband transition for IR detection and for reducing the device dark current. Figure 4.7 shows the dark current density versus bias voltage with temperature as a parameter (40 to 60 K) for this device, along with the 300 K window current. The thermal activation energy due to thermionic emission can be determined from figure 4.7 using Arrhenius plot. Figure 4.8 shows the variation of activation energy with bias at 40 K. As can be seen from figure 4.8 that the activation energy versus bias voltage follows a straight line, as expected from Eq.(4.3). From this figure the thermal activation energy at zero bias was found to be 72.1 meV, in excellent agreement with the 75.5 meV calculated from the $E_b - E_1 - E_F$. The spectral responsivity of this QWIP at 77 K under $\pm 2\text{V}$ is shown in figure 4.9. The responsivity peak was found to be at 14.7 μm , which is in excellent agreement with the calculated value when the exchange energy is taken into account. Figure 4.10 shows the variation of peak responsivity with bias at 40 K. As can be seen from this figure, the responsivity remains zero at very low bias voltages and increases rapidly for $|V_b| > 0.5\text{ V}$, which is the characteristics of the bound to bound state transition.

The detectivity can be expressed as

$$D_\lambda^* = R_i \sqrt{\frac{A_d \Delta f}{4eI_d g}} \quad (4.7)$$

where R_i is the responsivity, A_d is the device area, Δf is the band width, e is the electron charge, I_d is the dark current, g is the noise gain, which can be obtained by [17]

$$g(V) = \frac{I_d R_0}{\frac{kT}{e} N^2 \exp(\frac{\Delta E}{kT})} \quad (4.8)$$

where R_0 is the dynamic resistance at zero bias, N is the period number, k is the Boltzmann constant, ΔE is the barrier lowering, which is given by

$$\Delta E = e \sqrt{\frac{eV_b}{4l_i \pi \epsilon_0 \epsilon_r}} \quad (4.9)$$

where V_b is the bias voltage across one period, l_i is one period length, ϵ_0 is the free space permittivity, and ϵ_r is the dielectric constant.

The D^* of this device was calculated at 40 K, 2 V bias using Eqs. (4.7) - (4.9) and the measured responsivity and device dark current. The result yields a D^* of 1.12×10^{10} cm-Hz^{1/2} W⁻¹. This D^* value is reasonably good for a VLWIR QWIP with cutoff wavelength at 16.3 μ m. New VLWIR QWIP structures are currently being studied to further improve the device performance.

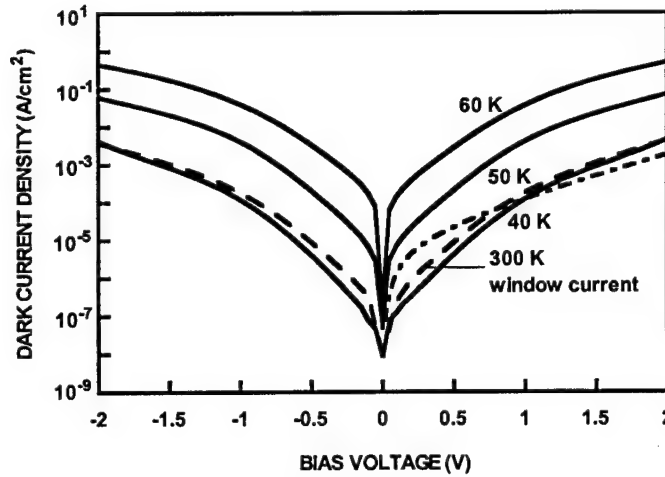


Figure 4.7 Measured dark current density versus bias voltage for the 14.7 μ m VLWIR QWIP. The dash-dotted line is the calculated dark current density at 40 K obtained from Eq.(4.3).

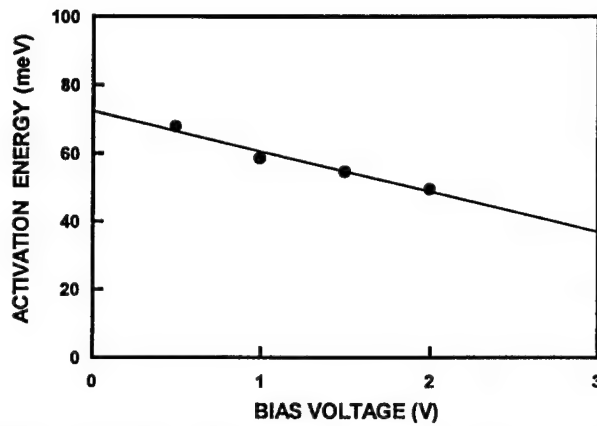


Figure 4.8 Activation energy versus bias voltage for the 14.7 μm VLWIR QWIP.

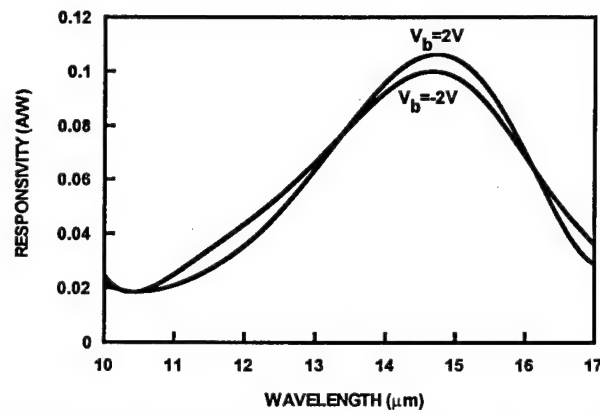


Figure 4.9 The spectral responsivity of the 14.7 μm VLWIR QWIP at $V_b = \pm 2\text{V}$ bias and 40K

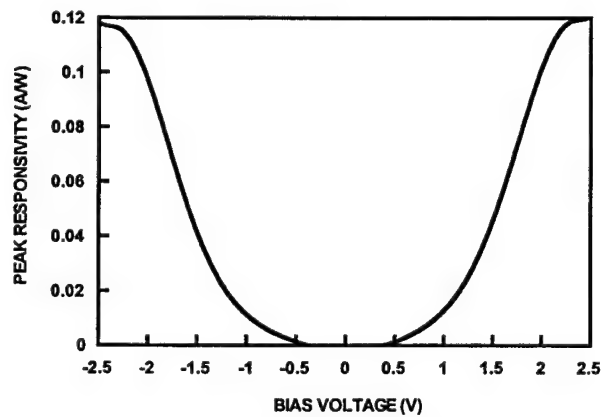


Figure 4.10 Variation of peak responsivity versus bias at 40 K for the 14.7 μm VLWIR QWIP.

4.5 Conclusions

In this chapter the latest development in VLWIR QWIPs has been discussed. We have investigated the design requirement, underlying fundamental device physics, multi-color QWIP including a VLWIR stack and several ways of reducing the dark current. We have also designed, fabricated, and characterized a VLWIR QWIP with cutoff wavelength at 16.3 μm . The device shows promising performance and improvement is under way with new device structures.

4.6 References

1. B.F. Levine, J. Appl. Phys. **74**, R1, (1993).
2. S.D. Gunapala and K.M.S.V. Bandara, Thin Films **21**, 113 (1995).
3. Sheng S. Li, Journal of the Chinese Institute of Electrical Engineering **2**, 37 (1995).
4. G. Sarusi, S.D. Gunapala, J.S. Park and B.F. Levine, J. Appl. Phys. **76**, 6001 (1994).
5. B.F. Levine, A. Zussman, J.M. Kuo and J. De Jong, J. Appl. Phys. **71**, 5130 (1992).
6. S.D. Gunapala, K.M.S.V. Bandara, B.F. Levine, G. Sarusi, D.L. Sivco and A.Y. Cho, Appl. Phys. Lett. **64**, 2288 (1994).
7. C.Y. Lee, M.Z. Tidrow, K.K. Choi, W.H. Chang, L.F. Eastman, F.J. Towner and J.S. Ahearn, J. Appl. Phys. **75**, 4731 (1994).
8. A.G.U. Perera, W.Z. Shen, S.G. Matsik, H.C. Liu, M. Buchanan and W.J. Schaff, Appl. Phys. Lett. **72**, 1596 (1998).
9. J. Chu, Sheng S. Li, A. Singh and P. Ho, Appl. Phys. Lett. **72**, 1664 (1998).
10. S. D. Gunapala, J. S. Park, G. Sarusi, T. L. Lin, J. K. Liu, P. D. Maker, R. E. A. Muller, C. A. Shott, and T. Hoelter, IEEE Trans. Electron. Devices **44**, 45 (1997).
11. B.F. Levine, C.G. Bethea, G. Hasnain, V.O. Shen, E. Pelve, R.R. Abbott and S.J.

- Hsieh, Appl. Phys. Lett. **56**, 851 (1990).
12. M.O. Vassell, Johnson Lee and H.F. Lockwood, J. Appl. Phys. **54**, 5206 (1983).
13. Lawrence West, "Spectroscopy of GaAs Quantum Wells", Ph. D. Thesis, July 1985.
14. K.M.S.V. Bandara, D.D. Coon, Byungsung O, Y.F. Lin and M.H. Francombe, Appl. Phys. Lett. **53**, 1931 (1988).
15. J.C. Chiang, Sheng S. Li, M.Z. Tidrow, P. Ho, M. Tsai and C.P. Lee, Appl. Phys. Lett. **69**, 2412 (1996).
16. M.Z. Tidrow, J.C. Chiang, Sheng S. Li and K.Bacher, Appl. Phys. Lett. **70**, 859 (1997).
17. D.C. Wang, G. Bosman and S.S. Li, Appl. Phys. Lett. **68**, 2532 (1997).

5. Quantum-Well Infrared Photodetectors With Digital Graded Superlattice Barrier For Long Wavelength and Broadband Detection

5.1 Introduction

Quantum well infrared photodetectors (QWIPs) have been widely investigated for multi-color and broadband infrared detection in the mid-wavelength infrared (MWIR) and long-wavelength infrared (LWIR) atmospheric spectral windows in the past decades [1-3]. The multi-stack structure is usually employed to obtain multi-color detection in the MWIR and LWIR wavebands [2-4]. In addition, voltage tunable QWIPs with asymmetrical quantum well structures have also been studied for multi-color detection [4-6]. The broadband infrared detection has been achieved by using a wide variety of device structures [5-10]. Levine *et al.* have reported a voltage tunable LWIR QWIP using graded barrier quantum wells to achieve large shifts in the peak detection wavelength, the spectral line-width, and the cutoff wavelength [10]. Duboz *et al.* have also studied the effect of asymmetrical linear graded barrier on the performance of GaAs/AlGaAs QWIPs [11]. In this work we report two novel high performance InGaAs/AlGaAs/GaAs QWIPs using digital graded superlattice barriers (DGSLB) to achieve the linearly graded band gap (or composition) across the barrier region of the QWIP. The new structures enable the broadband detection and significantly improve the responsivity of the device under positive bias operation. This band gap engineering approach has been widely used in III-V photonic devices for band gap variation and for enhancing device performance [12-13].

5.2 Device Design and Fabrication

In this work, two novel InGaAs/GaAs/AlGaAs QWIP structures using GaAs/AlGaAs digital graded superlattice barriers (DGSLB) were grown on the semi-

insulating GaAs substrates by using molecular beam epitaxy (MBE). The DGSLB structure was used to achieve the linearly graded barrier (i.e., linearly graded band gap or composition) in both devices. The standard MBE growth of the graded layer structure usually requires pausing the growth to change and stabilize the source temperature for the desired composition profile. As a result, it requires a longer growth time and may lead to more oxygen to be incorporated into the graded layer during the growth interruption. The compositionally digital-graded superlattice barriers (DGSLB) of the QWIP structures were grown using digital superlattice, which enable a stepwise linear composition grade to be formed without adjustment of the source temperature and the AlGaAs composition (i.e., using a fixed (15%) Al composition). The DGSLB structure can be obtained by using short-period superlattice structures with variable barrier/well thickness to change the Al mole fraction ratio and hence the energy band gap of the graded barrier. Adjusting the duty cycle can change the barrier/well thickness for each superlattice unit cell. Using the DGSLB structure without changing the source temperature setting greatly simplifies the growth procedure and yields excellent wafer quality. The DGSLB layers were formed by using five superlattice unit cells in series in which the thin GaAs/Al_{0.15}Ga_{0.85}As layers with a 20 Å period were repeated 5 times for each superlattice unit cell. The device structure for the broadband (BB-) DGSLB QWIP consists of a 50 Å In_{0.2}Ga_{0.8}As quantum well (Si doped to $7 \times 10^{17} \text{ cm}^{-3}$) and a 500 Å GaAs/Al_{0.15}Ga_{0.85}As DGSLB layer. Each superlattice unit cell in the DGSLB-layer has the combination of different barrier/well thicknesses (2.4/17.6, 4.8/15.2, 7.2/12.8, 9.6/10.4, and 12/8 Å) in order to obtain the target Al mole fractions of $x = 0.018, 0.036, 0.054, 0.072, \text{ and } 0.09$ from the substrate side for the stepwise linear graded barrier layer. In the double barrier (DB-) DGSLB QWIP, a thin (20 Å) undoped Al_{0.15}Ga_{0.85}As double barrier was grown between the DGSLB layers and the 88 Å In_{0.2}Ga_{0.8}As quantum well (Si doped to $7 \times 10^{17} \text{ cm}^{-3}$) to

confine the electron wave functions and to create a resonant state (E_5) with the graded superlattice barrier. The DGSLB layer used barrier/well thicknesses of 1.6/18.4, 3.2/16.8, 4.8/15.2, 6.4/13.6, and 8/12 Å for the target Al mole fractions of $x = 0.012, 0.024, 0.036, 0.048,$ and 0.06 in the $\text{Al}_x\text{Ga}_{1-x}\text{As}$ graded barrier layer for the DB-DGSLB QWIP. The 5000 Å contact layers (Si doped to $2 \times 10^{18} \text{ cm}^{-3}$) were grown at a substrate temperature of 600 °C, while the rest of the structure was grown at 510 °C to avoid indium (In) desorption from the InGaAs layers.

In order to characterize the device performance, test mesa structures with active area of $216 \times 216 \mu\text{m}^2$ were fabricated by using standard photolithography and wet chemical etching procedure. The AuGe/Ag/Au film was deposited by E-beam evaporation on the top and periphery of the mesa structure for ohmic contacts and annealed at 450 °C for 2 minutes. The test devices were polished to 45° facet on the GaAs substrates for backside illumination.

5.3 Results and Discussions

Figures 5.1(a) and (b) show the dark current density as a function of the applied bias measured at $T = 35, 50, 60,$ and 77K along with the 300K background window current with a 180° field of view (FOV) and the schematic conduction band diagram for the BB- and DB-DGSLB QWIPs, respectively. The dark current-voltage (I-V) and the spectral response characteristics are highly asymmetrical under positive and negative bias conditions while the bottom contact layer was grounded, which is attributed to the change in the effective barrier height under negative and positive biases. In both devices we have observed a much higher dark current and peak responsivity under positive bias condition. This is due to the barrier lowering of the DGSLB and the effect of electron launching under positive bias condition. The BB-DGSLB QWIP is under background limited

performance (BLIP) between -1V and $+0.75\text{V}$ at $T = 35\text{K}$, and the BLIP temperature was found at 55K . As for the DB-DGSLB QWIP, the device is under BLIP between -2V and $+0.35\text{V}$ at $T = 50\text{K}$. As shown in Fig. 5.1 (a) and (b), the dotted lines in the schematic conduction band diagrams of the BB- and DB-DGSLB QWIPs denote the effective barrier height for each superlattice unit cell (5 periods, 20 \AA /period) in the DGSLB layers. Therefore, the digital graded superlattice barrier (DGSLB) can create a staircase-like barrier in these BB- and DB-DGSLB QWIP structures. For the BB-DGSLB QWIP, the E_1 - E_4 , E_1 - E_5 , and E_1 - E_6 transitions lead to the broadband spectral response under positive bias condition, while only transitions from the E_1 - E_6 states were observed under negative bias because the photo-generated carriers need to surmount the abrupt side of the barrier layers. Under positive bias condition, the effective barrier will decrease gradually with increasing bias to the lowest superlattice barrier height, and the bound states aligned by the DGSLB at zero bias will be the pseudo-continuum states over the DGSLB layers. Thus, the broadband response can be achieved by the bound-to-pseudo-continuum (BTPC) state transitions under positive bias condition. On the contrary, the effective barrier height for the photo-excited electron transport will be at its maximum under negative bias condition, and the slope of the DGSLB will be much steeper than under positive biases. As a result, the capture probability of the photo-excited electrons due to the bound-to-bound (BTB) transitions will be increased and normal spectral response (with narrower spectral width) is expected under negative bias condition. For the DB-DGSLB QWIP, the broadband response was not observed in this device because the wave function for the E_5 - state is strongly confined by the thin undoped $\text{Al}_{0.15}\text{Ga}_{0.85}\text{As}$ double-barrier and resonantly coupled to the wave functions of the E_5 - state in the DGSLB region. Thus, normal spectral response with identical peak detection

wavelength at 12 μm due to the E_1 to E_5 state transitions was obtained under both negative and positive biases for this device.

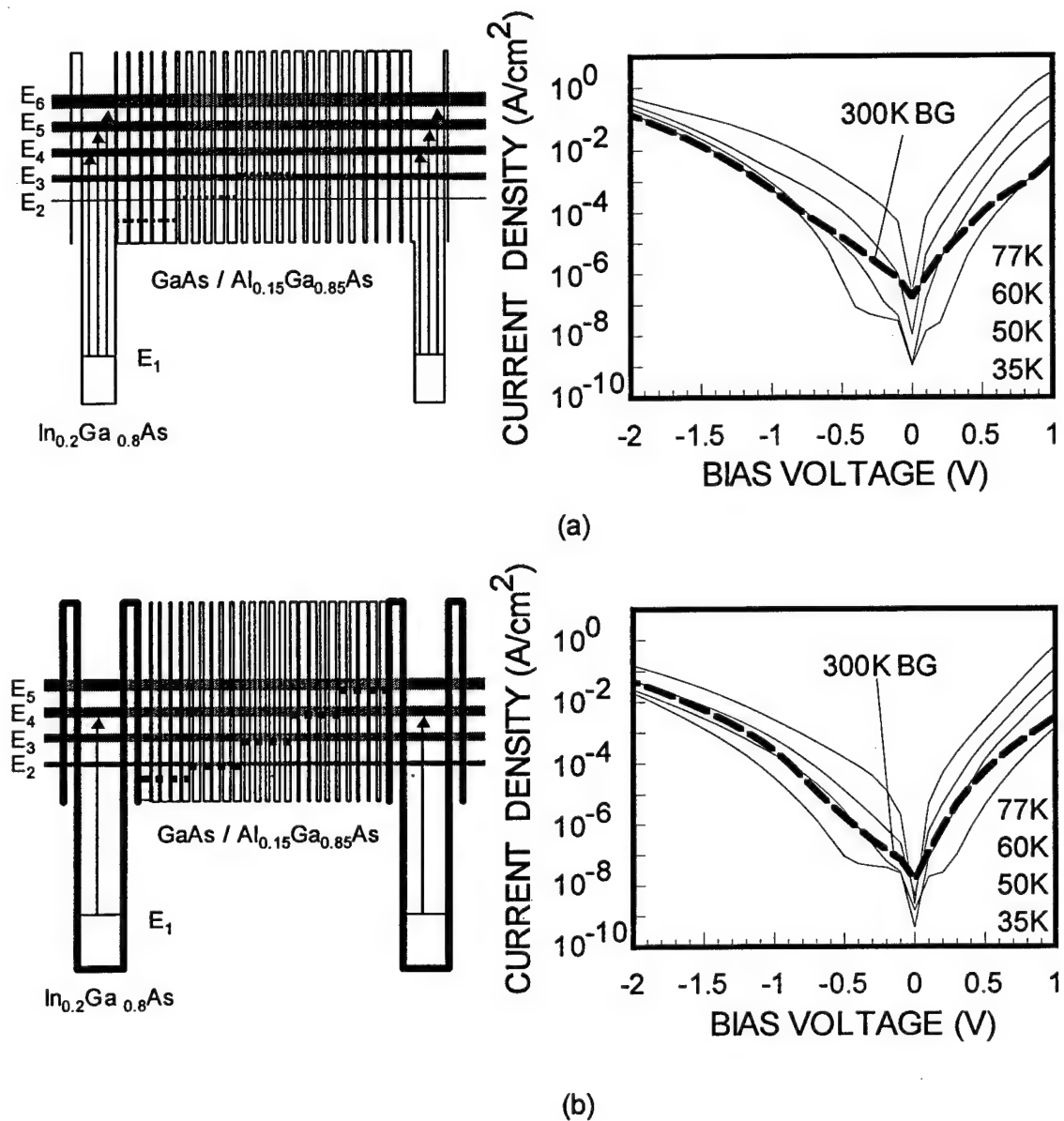


Figure 5.1 The dark current density versus bias voltage and the schematic conduction band diagram for (a) the BB-DGSLB QWIP and (b) the DB-DGSLB QWIP using InGaAs/AlGaAs/GaAs material systems grown on GaAs.

The spectral response was measured at $T = 35\text{K}$ for both the BB- and DB-DGSLB QWIPs by using an 1/8 m grating monochromator, a calibrated blackbody IR source ($T = 1273\text{K}$), and a closed cycle liquid helium cryostat at 200 Hz chopped frequency. Figure 5.2 shows the spectral responsivity of the BB- DGSLB QWIP at $T = 35\text{K}$ under (a) negative and (b) positive bias conditions. The peak wavelength was shifted slightly from $11\text{ }\mu\text{m}$ to $10.8\text{ }\mu\text{m}$ between -0.75V and -1.25V under negative bias condition. The absolute responsivity increases with the applied bias due to the increase in photoconductive gain with increasing bias. The peak responsivities at $\lambda_p = 10.8\text{ }\mu\text{m}$ and $9.8\text{ }\mu\text{m}$ were found to be 0.57 A/W and 1.07 A/W at $V_b = -1.25\text{V}$ and $+0.75\text{V}$, respectively. It is noted that a very broad spectral bandwidth from 7 to $16\text{ }\mu\text{m}$ was obtained under positive bias condition in the BB-DGSLB QWIP. The full-width half-maximum (FWHM) spectral bandwidth of this device at $V_b = -1.25\text{V}$ was found to be $\Delta\lambda/\lambda_p = 13\%$, while FWHM spectral bandwidths at $V_b = +0.75\text{V}$ and $+0.5\text{V}$ were found to be $\Delta\lambda/\lambda_p = 62\%$ and 54% , respectively. This broadband detection feature was attributed to the formation of pseudo-continuum states by the overlapping of E_4 , E_5 , and E_6 state wave functions, which enables the broadband detection from the E_1 to the E_4 , E_5 , and E_6 quasi-continuum states transitions under positive bias condition.

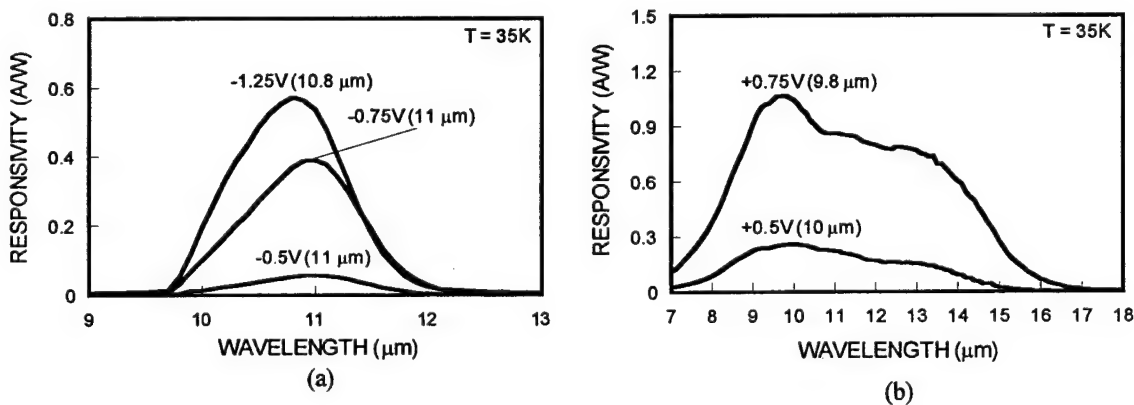


Figure 5.2 The spectral responsivity of the BB-DGSLB QWIP measured at $T = 35\text{K}$ under (a) negative and (b) positive biases.

Figure 5.3 shows the spectral responsivity of the DB-DGSLB QWIP at $T = 35\text{K}$ under (a) negative and (b) positive bias conditions. The maximum peak responsivity at $\lambda_p = 11.8\text{ }\mu\text{m}$ was found to be 0.28 A/W at $V_b = -1.5\text{V}$ and $T = 35\text{K}$. However, the spectral responsivity was dramatically increased under positive bias condition due to the graded barrier lowering and electron launching effect. The peak responsivity at $V_b = +1\text{V}$ was 3 A/W at $\lambda_p = 12\text{ }\mu\text{m}$ and $T = 35\text{K}$. The peak detection wavelength for this device was due to the $E_I - E_5$ state transitions. Values of background limited performance (BLIP) detectivity (D^*_{BLIP}) for the BB-DGSLB QWIP were found to be $7.2 \times 10^9\text{ cm-Hz}^{1/2}/\text{W}$ at $V_b = -0.75\text{V}$, $\lambda_p = 11\text{ }\mu\text{m}$, and $1.3 \times 10^{10}\text{ cm-Hz}^{1/2}/\text{W}$ at $V_b = +0.75\text{V}$, $\lambda_p = 9.8\text{ }\mu\text{m}$, respectively. The BLIP detectivities (D^*_{BLIP}) for the DB-DGSLB QWIP were found to be $5.8 \times 10^9\text{ cm-Hz}^{1/2}/\text{W}$ at $V_b = -1.5\text{V}$ and $\lambda_p = 11.8\text{ }\mu\text{m}$ and $1.9 \times 10^{10}\text{ cm-Hz}^{1/2}/\text{W}$ at $V_b = +1\text{V}$, $\lambda_p = 12\text{ }\mu\text{m}$, respectively.

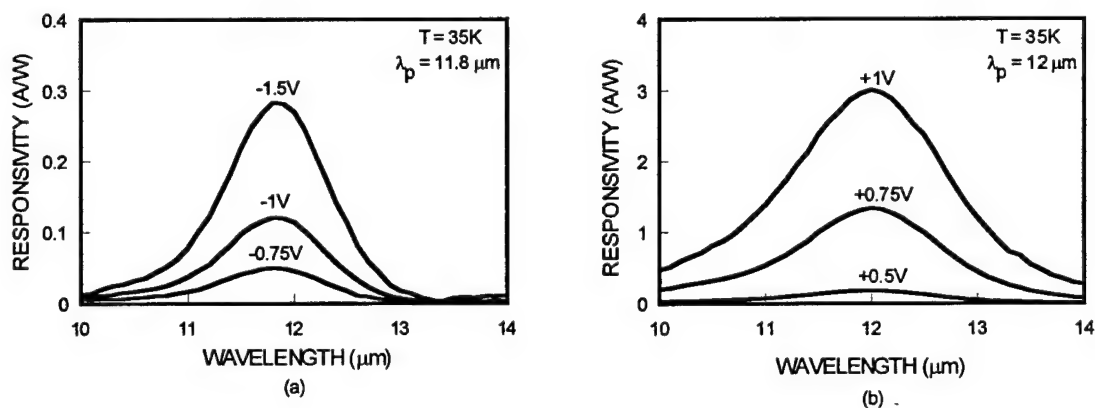


Figure 5.3 The spectral responsivity of the DB-DGSLB QWIP measured at $T = 35\text{K}$ under (a) negative and (b) positive biases.

5.4 Conclusions

In conclusion, we have demonstrated a novel broadband (BB-) InGaAs/AlGaAs/GaAs QWIP using digital graded superlattice barrier (DGSLB) and a double-barrier (DB-) InGaAs/AlGaAs/GaAs/AlGaAs DGSLB QWIP for LWIR and broadband detection. For the BB-DGSLB QWIP, the peak responsivity at $\lambda_p = 9.8 \mu\text{m}$ was found to be 1.07 A/W at $V_b = +0.75\text{V}$ and $T = 35\text{K}$, with a corresponding D^*_{BLIP} of $1.3 \times 10^{10} \text{ cm} \cdot \text{Hz}^{1/2}/\text{W}$. A very broad spectral response bandwidth covering the wavelength from $7 \mu\text{m}$ to $16 \mu\text{m}$ was obtained under positive bias condition for this device. The FWHM spectral bandwidth at $V_b = +0.75\text{V}$ and $+0.5\text{V}$ were found to be $\Delta\lambda/\lambda_p = 62\%$ and 54% , respectively. As for the DB-DGSLB QWIP, a very large spectral responsivity and BLIP detectivity (i.e., $R_i = 3 \text{ A/W}$ and $D^*_{BLIP} = 1.9 \times 10^{10} \text{ cm Hz}^{1/2}/\text{W}$) was obtained at $V_b = +1\text{V}$ and $\lambda_p = 12 \mu\text{m}$. Excellent device performance was achieved for both QWIPs, which was attributed to the use of digital graded superlattice barriers (DGSLB) to form the linearly graded barrier layer in both device structures, enabling these DGSLB QWIPs to achieve broadband detection, high peak responsivity, and wavelength tunability by the applied bias.

5.5 References

1. B. F. Levine, J. Appl. Phys., **74**, R1, (1993).
2. J. C. Chiang, Sheng S. Li, and A. Singh, Appl. Phys. Lett., **71**(24), pp. 3546-3548, 14 October, (1996).
3. M. Z. Tidrow, Xudong Jiang, Sheng S. Li, and K. Bacher, Appl. Phys. Lett., **74**(9), pp. 1335-1337, 1 March, (1999).
4. Jung-Chi Chiang, Sheng S. Li, M. Z. Tidrow, P. Ho, M. Tsai, and C. P. Lee, Appl. Phys. Lett., **69**(16), pp. 2412-2414, 14 October, (1996).
5. H. C. Liu, J. Li, J. R. Thompson, Z. R. Wasilewski, M. Buchanan, and J. G. Simmons, IEEE Trans. Electron Devices, **14**, 566 (1993).

6. L. C. Lenchyshyn, H. C. Liu, M. Buchanan, and Z. R. Wasilewski, *J. Appl. Phys.*, **79**(6), pp. 3307-3311, 15 March, (1996).
7. Sheng S. Li, J. Chu, J. C. Chiang, J. H. Lee, and A. Singh, *Proc. of SPIE*, vol. **3629**, pp. 138-146, (1999).
8. S. V. Bandara, S. D. Gunapala, J. K. Liu, E. M. Luong, J. M. Mumolo, W. Hong, D. K. Sengupta, and M. J. Mckelvey, *Appl. Phys. Lett.*, **72**(19), pp. 2427-2429, 11 May, (1998).
9. Y. Zhang, N. Baruch and W. I. Wang, *Electronics letters*, vol. **29**(2), pp. 213-214, 21 January, (1993).
10. B. F. Levine, C. G. Bethea, V. O. Shen, and R. J. Malik, *Appl. Phys. Lett.*, **57**(4), pp. 383-385, 23 July, (1990).
11. J. Y. Duboz, L. Saminadayar, and J. M. Gerard, *J. Appl. Phys.*, **78**(4), pp. 2803-2807, 15 August, (1995).
12. Wei Gao, Paul R. Berger, George J. Zyzdik, Henry M. O'Bryan, Deborah L. Sivco, and Alfred Y. Cho, *IEEE Transaction of Electronic Devices*, vol. **44**(12), pp. 2174-2179, December 12, (1997).
13. D. H. Lee, Sheng S. Li, N. J. Sauer, and T. Y. Chang, *Appl. Phys. Lett.*, **54**(19), pp. 1863-1865, 8 May, (1989).

6. Multi-color, Broadband Quantum Well Infrared Photodetectors With Linear- Graded Barrier

6.1 Introduction

Quantum well infrared photodetectors (QWIPs) have been widely investigated for detection in the 3-5 μm mid-wavelength infrared (MWIR) and 8-14 μm long-wavelength infrared (LWIR) atmospheric spectral windows [1-4]. The mature III-V compound semiconductor growth technology and the design flexibility of device structures have led to the rapid development of various QWIP structures for a wide variety of IR imaging array applications. Multi-color QWIPs using multi-stack and voltage-tunable asymmetrical coupled quantum well structures have been reported [2,4]. In addition, broadband QWIPs covering the 8-14 μm atmospheric spectral window have also been demonstrated by using stacked quantum wells with different well width and depth [5,6] and asymmetrical quantum well structure [7,8]. Recently, a novel QWIP using digital graded superlattice barrier (DGSLB) has been reported for broadband detection in the 7 - 14 μm waveband [9]. Here we report the demonstration of a high sensitivity two-stack $\text{In}_{0.26}\text{Ga}_{0.74}\text{As}/\text{Al}_x\text{Ga}_{1-x}\text{As}$ broadband (BB-) QWIP with a linear- graded barrier (LGB) and $\text{Al}_{0.15}\text{Ga}_{0.85}\text{As}/\text{In}_{0.26}\text{Ga}_{0.74}\text{As}/\text{Al}_{0.15}\text{Ga}_{0.85}\text{As}$ double-barrier (DB-) LGB QWIP for multicolor and broadband long wavelength infrared (LWIR) detection.

6.2 Device Design and Fabrication

The BB- and DB- linear- graded barrier (LGB) QWIP structures were grown sequentially on the semi-insulating GaAs substrate by using molecular beam epitaxy (MBE). The top stack is a BB- LGB QWIP, which consists of 15 periods of a 45 \AA $\text{In}_{0.26}\text{Ga}_{0.74}\text{As}$ quantum well (Si-doped to $7 \times 10^{17} \text{ cm}^{-3}$) and a 500 \AA linear- graded

barrier of $\text{Al}_x\text{Ga}_{1-x}\text{As}$ with the Al mole fraction (x) varying from 1.8% to 9%. The bottom stack is a DB- LGB QWIP, which has two thin (20 Å) undoped $\text{Al}_{0.15}\text{Ga}_{0.85}\text{As}$ barrier layers added on both sides of the 72 Å $\text{In}_{0.26}\text{Ga}_{0.74}\text{As}$ quantum well (Si-doped to $7 \times 10^{17} \text{ cm}^{-3}$) for confinement of the electron wave functions in the E_5 state in the quantum well, which is resonantly coupled to the $\text{Al}_x\text{Ga}_{1-x}\text{As}$ graded barrier layer. 15 periods of quantum well were grown for the bottom DB-LGB QWIP stack. Finally, the ohmic contact layers (Si-doped to $2 \times 10^{18} \text{ cm}^{-3}$) with different thicknesses (3000 Å, 7000 Å, and 5000 Å) were grown on the top side of the BB-LGB QWIP stack and on the bottom side of the DB-LGB QWIP stack, and between the two stacks, respectively.

The test mesa structure has an active area of $216 \times 216 \mu\text{m}^2$, which was processed using standard photolithography and wet chemical etching procedures. The AuGe/Ag/Au (300 Å/1000 Å/1500 Å) films were deposited on the top and the periphery of the mesa structure for ohmic contact metalization. A 45° facet was polished on the GaAs substrate for back- side illumination into the QWIP active region.

6.3 Results and Discussions

Figure 6.1 (a) and (b) shows the dark I-V curves measured at $T = 35, 50, 60$, and 77K for the BB- and DB-LGB QWIPs, respectively. At small biases, the dark current of the DB-LGB QWIP is lower than that of the BB-LGB QWIP, which is attributed to the use of a thin double-barrier in this QWIP structure for current suppression. At higher biases, the DB-layer is no longer effective in blocking the dark current tunneling through the lower excited states in the quantum well, and the dark current in both QWIPs is nearly identical. The highly asymmetrical dark current characteristics can be attributed to the use of the LGB structure which creates an asymmetrical barrier in both devices under positive and negative bias condition.

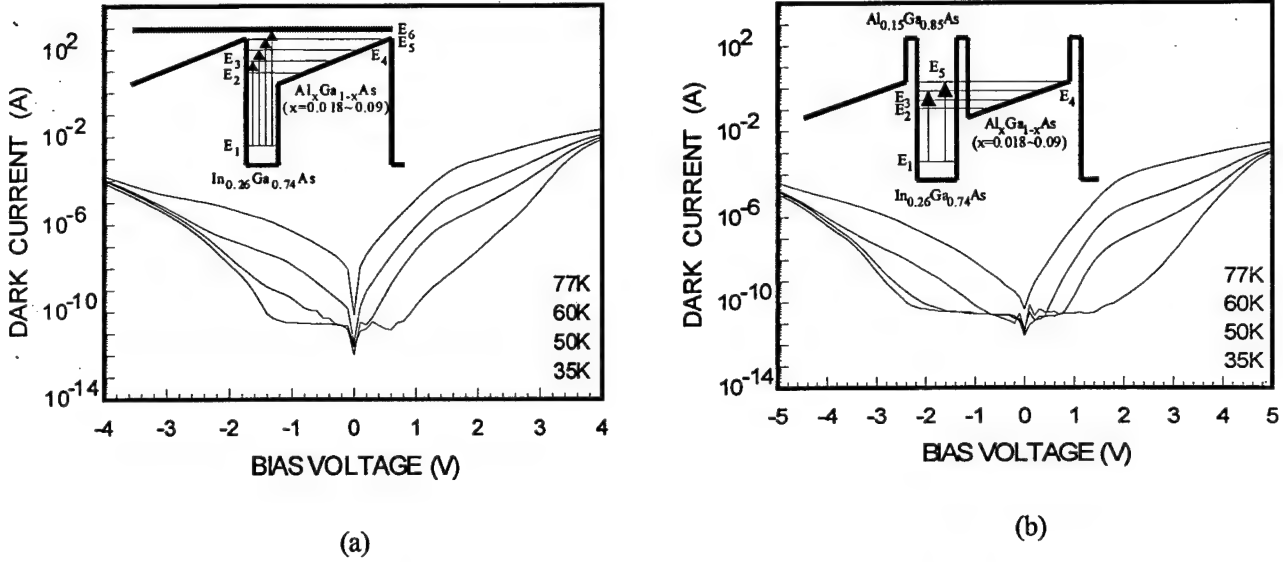


Figure 6.1 Dark current versus bias voltage curves for (a) the BB-LGB QWIP and (b) the DB-LGB QWIP. The insets are the schematic conduction band diagrams.

The insets in Fig. 6.1 show the schematic conduction band diagrams and the intersubband transition schemes for (a) the BB- and (b) the DB- LGB QWIPs, respectively. The photo-generated carrier transport for the BB- and DB-LGB QWIP is strongly dependent on the polarity of the applied bias. Under positive bias condition, the barrier height of the LGB layer was decreased with increasing bias and the photo-excited electrons from the longer wavelength photons can easily transport through the barrier and reach the contacts. The broadband (BB) detection for the top LGB- QWIP stack was realized by the superposition of the photo-responses due to the transitions from the E_1 to the E_3 , E_4 , E_5 , and E_6 states under positive bias condition. On the other hand, the barrier height of the LGB will remain unchanged under negative bias condition, and the longer-wavelength photo-responses due to the E_1 to E_3 and E_4 states transitions were suppressed. As a result only two photo-response peaks due to the E_1 to E_5 and E_6 states transitions were observed under negative bias condition. For the bottom DB-LGB QWIP stack, the large peak responsivity was attributed to the use of thin $\text{Al}_{0.15}\text{Ga}_{0.85}\text{As}$ double- barrier to confine the electron wave functions of the E_5 state, which results in a stronger

intersubband absorption for the E_1 to E_5 state transition. Normal narrow spectral response was observed for this device under both the positive and negative bias conditions.

The spectral response measurements were performed on the QWIP devices by using a grating monochromator, a calibrated blackbody IR source ($T = 1273\text{K}$), and a closed cycle liquid helium cryostat, measured at 200 Hz chopper frequency and with a 45° facet backside illumination.

Figure 6.2 shows the spectral responsivity of the BB-LGB QWIP at 35K under (a) negative and (b) positive bias conditions. As shown in Fig 6.2 (a), under negative bias condition, the main response peak, which occurs at $9.9\text{ }\mu\text{m}$, is due to the E_1 to E_5 state transition, and a smaller secondary response peak at $8\text{ }\mu\text{m}$ is due to the E_1 to E_6 state transition. The maximum peak responsivity for the $9.9\text{ }\mu\text{m}$ peak is 1.61 A/W at $V_b = -3.5\text{ V}$ and $T = 35\text{K}$. The spectral responsivity increases with increasing bias voltage. The inset in Fig 6.2 (a) shows the linear dependence of the peak wavelength on the applied bias for both the E_1 - E_5 and E_1 - E_6 transitions under negative bias condition, which is attributed to the quantum confined Stark shift effect in these states. A blue shift in the peak wavelength with applied bias was obtained for both peaks, varying from 10.2 to $9.9\text{ }\mu\text{m}$ and 8.5 to $7.5\text{ }\mu\text{m}$ for the E_1 - E_5 and E_1 - E_6 states transitions, respectively. As shown in Fig 6.2 (b), under positive bias condition, the peak responsivity at $\lambda_p = 11.9\text{ }\mu\text{m}$ was found to be 1.75 A/W at $+2.75\text{V}$ and $T = 35\text{K}$. Three response peaks at $\lambda_p = 8.9, 10.2,$ and $11.9\text{ }\mu\text{m}$ were observed, which were attributed to the E_1 to $E_4, E_5,$ and E_6 states transitions. The full-width half-maximum (FWHM) spectral bandwidth of this device at $+2.75\text{V}$ and $T = 35\text{K}$ was $\Delta\lambda/\lambda_p = 52\%$. A broadband spectral response covered the wavelength from 6.5 to $16\text{ }\mu\text{m}$ under positive bias condition was obtained in this device by the superposition of the photo- responses due to the E_1 to $E_6, E_5, E_4,$ and E_3 states

transitions. The E_1 to E_6 and E_5 state transitions were the dominant response peaks at lower biases ($V_b < +1V$), while the E_1 to E_4 and E_3 state transitions can only be detected at higher bias voltages. However, the contribution of the E_1 to E_3 state transition to the broadband detection is much smaller than other transitions at higher positive bias voltages.

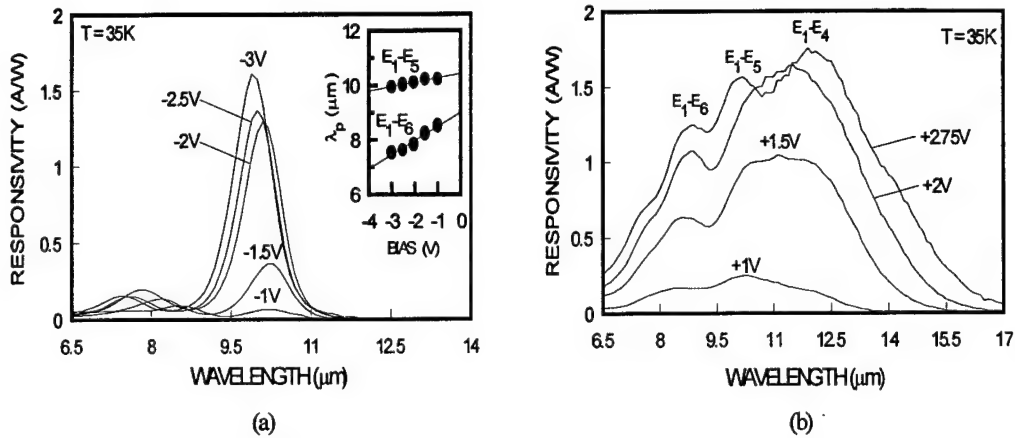


Figure 6.2 Spectral responsivity of the BB-LGB QWIP measured at $T = 35K$ under (a) negative and (b) positive bias conditions. The inset in (a) shows the linear dependence of the peak wavelength with the applied bias.

Figure 6.3 shows the spectral responsivity measured at $T = 35K$ for the bottom DB-LGB QWIP stack under (a) negative and (b) positive bias conditions. The peak responsivity due to the E_1 to E_5 state transition at $T = 35K$ and $-4.5V$ was $1.23 A/W$ with peak detection wavelength at $\lambda_p = 9.2 \mu m$. A very high responsivity of $4.38 A/W$ at $\lambda_p = 9.2 \mu m$ was obtained at $+3.5V$ and $T = 35K$. The enhancement of the responsivity for this response peak is attributed to the combined use of the DB and LGB structure for the E_1 to E_5 state transition. The use of an enlarged high-strain InGaAs quantum well with smaller electron effective mass will also contribute to the enhanced intersubband absorption. The absorption quantum efficiency (η) will increase with increasing absorption coefficient. In addition, the photoconductive gain (g) can also be increased due to lowering of the electron capture probability (p_c) by the smaller electron effective mass. As a result, the responsivity of the BB- and DB- LGB QWIPs was greatly increased due to the increase

of the collection efficiency ($\eta_c = \eta_g$) in both devices. The FWHM spectral bandwidth under positive bias was found twice broader than under negative bias since the E_1 - E_4 state transition for the longer wavelength detection can only be obtained under positive bias condition. The FWHM bandwidth at +3.5V was $\Delta\lambda/\lambda_p = 27\%$ while the FWHM bandwidth at -4.5V was $\Delta\lambda/\lambda_p = 11\%$. The E_1 - E_4 state transition was the dominant response peak at lower positive biases ($\leq +2.5V$), while the E_1 - E_5 state transition becomes the dominant response peak at higher positive biases ($\geq +3V$). The responsivity was increased substantially with increasing bias voltage under positive bias condition.

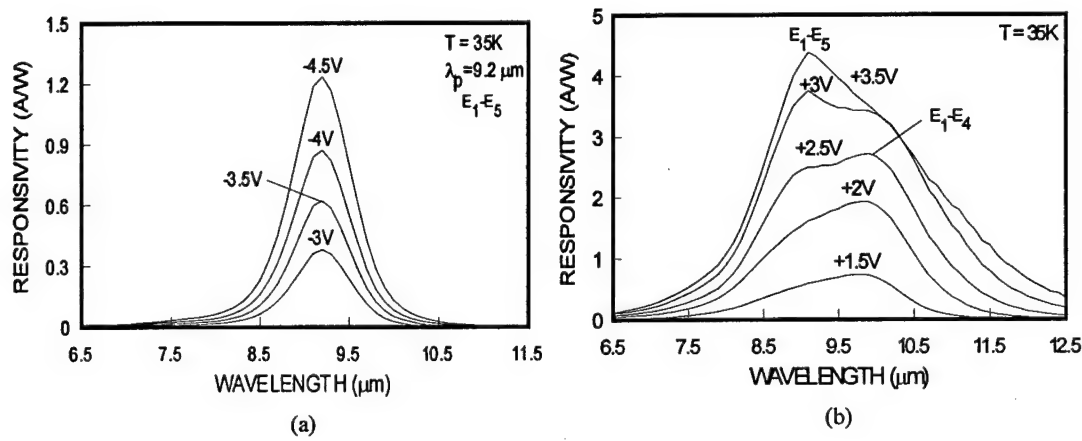


Figure 6.3 Spectral responsivity of the DB-LGB QWIP measured at $T = 35K$ under (a) negative and (b) positive bias conditions.

Calculations of the detectivity for the BB- and DB-LGB QWIPs were carried out using the measured dark current and the peak responsivity under non-BLIP (background limited performance) condition [10]. The peak detectivity for the BB-LGB QWIP was found to be $9.73 \times 10^{11} \text{ cm-Hz}^{1/2}/\text{W}$ at $-1.5V$, $\lambda_p = 10.2 \mu\text{m}$, and $35K$, while the peak detectivity at $+1V$ was $6.11 \times 10^{11} \text{ cm-Hz}^{1/2}/\text{W}$ at $10.3 \mu\text{m}$ and $35K$. For the DB-LGB QWIP, the peak detectivity at $-2.5V$ was $4.8 \times 10^{11} \text{ cm-Hz}^{1/2}/\text{W}$ at $9.2 \mu\text{m}$, and $35K$, while the peak detectivity at $+1.5V$ was $5.01 \times 10^{12} \text{ cm-Hz}^{1/2}/\text{W}$ at $9.8 \mu\text{m}$, and $35K$.

6.4 Conclusions

In conclusion, we have demonstrated a high sensitivity two-stack InGaAs/AlGaAs linear-graded barrier (LGB) QWIP for multicolor and broadband (BB) long wavelength detection and the double-barrier (DB-) AlGaAs/InGaAs/AlGaAs LGB QWIP for LWIR detection. A broadband detection was achieved from 6.5 to 16 μm at +2.75V and $T = 35\text{K}$ for the top BB-LGB QWIP stack. The peak wavelength is tunable with applied bias under negative bias condition due to the quantum confined Stark effect. Large peak responsivity and high non-BLIP detectivity were obtained at 35K for both the BB- and DB- LGB QWIPs reported here.

6.5 References

1. M. Z. Tidrow, K. Bacher, Appl. Phys. Lett. **69**, 3396 (1996).
2. J. C. Chiang, Sheng S. Li, and A. Singh, Appl. Phys. Lett. **71**, 3546 (1997).
3. S. Y. Wang and C. P. Lee, J. Appl. Phys. **82**, 2680 (1997).
4. X. D. Jiang, Sheng S. Li, and M. Z. Tidrow, IEEE Transaction on Quantum Electronics vol. **35**, 1685 (1999).
5. S. V. Bandara, S. D. Gunapala, J. K. Liu, E. M. Luong, J. M. Mumolo, W. Hong, D. K. Sengupta, and M. J. Mckelvey, Appl. Phys. Lett. **72**, 2427 (1998).
6. J. Chu, Sheng S. Li, and A. Singh, IEEE Transaction on Quantum Electronics vol. **35**, 312 (1999).
7. B. F. Levine, C. G. Bethea, V. O. Shen, and R. J. Malik, Appl. Phys. Lett. **57**, 383 (1990).
8. J. Y. Duboz, L. Saminadayar, and J. M. Gerard, J. Appl. Phys. **78**, 2803 (1995).
9. Jung-Hee Lee, Sheng S. Li, M. Z. Tidrow, W. K. Liu, and K. Bacher, Appl. Phys. Lett. **75**, 3207 (1999).
10. Daniel C. Wang, Gijs Bosman, and Sheng S. Li, Appl. Phys. Lett. **68**, 2532 (1996).

7. Enhancing the Quantum Efficiency of a QWIP by Using Photonic Crystal (PC)

7.1 Introduction

A photonic crystal is comprised of a periodic lattice of high and low refractive index materials and can modify the characteristics of light propagating within it. A well-known example of photonic crystal is the quarter-wave reflector, which is a one-dimensional multi-layer structure that has a frequency range for which all light incident upon it will be reflected and hence forms a band gap for photons within a specified frequency range. The gap is proportional to the difference in the refraction index of the two alternative materials composing the quarter-wave reflector. A defect in the photonic crystal, such as a vacancy on a lattice site can form deep levels to trap photons. The photonic crystals can be used to produce the world's smallest photonic components, such as thresholdless microcavity laser. We will explore the use of photonic crystal in quantum well infrared photodetectors to increase the quantum efficiency of QWIP and to increase the operating temperature of QWIP accordingly.

A disadvantage of conventional QWIP is that its quantum efficiency is too low compared to MCT detector. To improve the quantum efficiency, a grating + QWIP + photonic crystal structure is proposed: Normal incident light goes through substrate, photonic crystal and QWIP, while it hits the grating, the light will be scattered into different directions; the scattered light will be reflected by the photonic crystal. In this structure the light can travel through QWIP many times and significantly increase the quantum efficiency. The electromagnetic (EM) field inside grating can be treated by modal expansion method. The EM field in the QWIP and photonic crystal can be treated by transfer matrix method. Since inside the QWIP part of the light will be absorbed. As a result, the refractive index in the QWIP will be a complete one.

By properly calculating the power of electromagnetic field at the two sides of QWIP, one can obtain the power absorbed by the Q WIP and obtain the quantum efficiency by dividing the absorbed power by incident power. By changing the structure parameters, one can see how quantum efficiency varies with these parameters and get optimal structure parameters.

7.2 Theoretical Consideration

7.2.1 Reflecting and Refracting Through a Multi-layer Film

Figure 7.1 shows schematically the reflection and refraction of light in a multi-layer film.

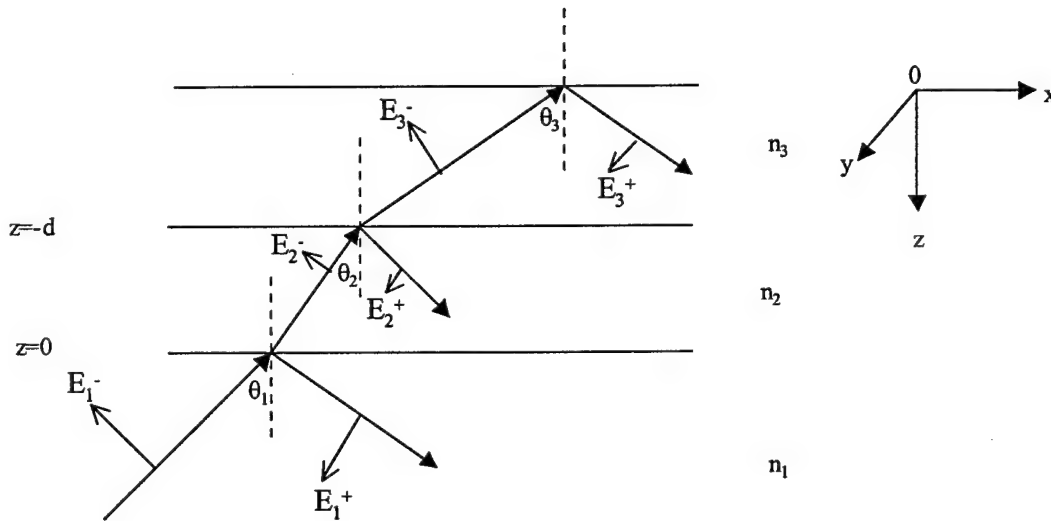


Figure 7.1 Schematic illustration of reflection and refraction of light in a multi-layer film.

In each layer, there are two electromagnetic waves: one incident toward the interface and one away from the interface. We consider a TM wave and use a coordinate system as shown in figure 7.1, some relevant quantities are listed in this figure. By applying Maxwell's equations and boundary conditions, we can obtain

$$\begin{pmatrix} E_1^- \\ E_1^+ \end{pmatrix} = \frac{1}{t_{12}} \begin{pmatrix} 1 & r_{12} \\ r_{12} & 1 \end{pmatrix} \begin{pmatrix} E_2^- \\ E_2^+ \end{pmatrix} \quad (7.1)$$

$$\begin{pmatrix} E_2^- \\ E_2^+ \end{pmatrix} = \frac{1}{t_{23}} \begin{pmatrix} e^{i\delta_2} & r_{23}e^{i\delta_2} \\ r_{23}e^{-i\delta_2} & e^{-i\delta_2} \end{pmatrix} \begin{pmatrix} E_3^- \\ E_3^+ \end{pmatrix} \quad (7.2)$$

where

$$r_{ij} = \frac{n_i \cos(\theta_j) - n_j \cos(\theta_i)}{n_j \cos(\theta_i) + n_i \cos(\theta_j)} \quad (7.3a)$$

$$t_{ij} = \frac{2n_i \cos(\theta_i)}{n_j \cos(\theta_i) + n_i \cos(\theta_j)} \quad (7.3b)$$

$$\delta_i = \frac{2\pi}{\lambda_0} n_i d_i \cos(\theta_i) \quad (7.3c)$$

λ_0 is the photon wavelength in vacuum and d_i is the thickness of the i-th layer.

If we have N period films with alternative refractive index, for example, layer 2 and 3

shown in figure 7.1 are repeated N times, we will get

$$\begin{pmatrix} E_1^- \\ E_1^+ \end{pmatrix} = S_1 S_2 S_3 S_2 S_3 \dots S_2 S_3 S_f \begin{pmatrix} E_f^- \\ E_f^+ \end{pmatrix} \quad (7.4)$$

S_i is the scatter matrix for each composite layer, and finally we get

$$\begin{pmatrix} E_1^- \\ E_1^+ \end{pmatrix} = \begin{pmatrix} S_{11} & S_{12} \\ S_{21} & S_{22} \end{pmatrix} \begin{pmatrix} E_f^- \\ E_f^+ \end{pmatrix} \quad (7.5)$$

The transmission coefficient is defined as

$$T = \left| \frac{E_f^-}{E_1^-} \right|^2 \quad (7.6)$$

7.2.2 Grating Coupler

Let's consider a lamellar grating, as schematically show in Fig. 7.2.

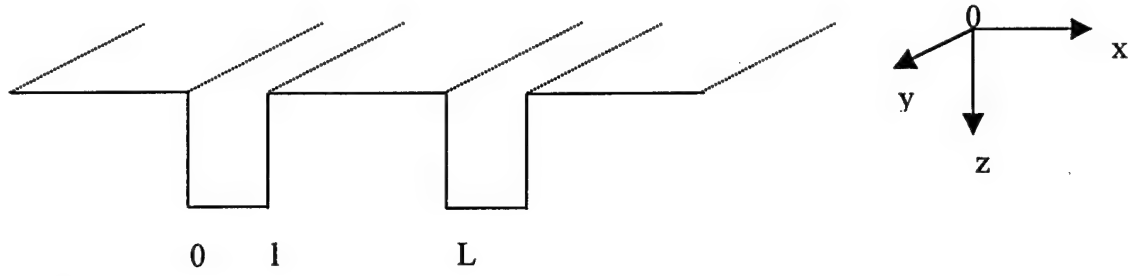


Figure 7.2 Schematic illustration of lamellar grating.

l is the groove width and L is the grating period. In the $z > 0$ half space, the x-component of the electric field for TM waves can be written as:

$$\begin{aligned} E_x^+ &= \frac{1}{\sqrt{L}} e^{i[\alpha_r x - \beta_r z]} + \sum_{p=-\infty}^{+\infty} S_p^r \frac{1}{\sqrt{L}} e^{i[\alpha_p x + \beta_p z]} \\ &= R_r(x, z) + \sum_{p=-\infty}^{+\infty} S_p^r R_p(x, z) \end{aligned} \quad (7.7)$$

Where

$$R_r(x, z) = \frac{1}{\sqrt{L}} e^{i(\alpha_r x - \beta_r z)} \quad (7.7a)$$

Is the r -th incident wave, and

$$R_p(x, z) = \frac{1}{\sqrt{L}} e^{i[\alpha_p x + \beta_p z]} \quad (7.7b)$$

is the p -th scattered wave.

For $z < 0$,

$$E_x^- = \sum_{n=0}^{\infty} C_n^r \sqrt{\frac{2 - \delta_{n0}}{l}} \cos \frac{n\pi x}{l} \sin[\mu_n(z + h)] \Theta(x) \Theta(l - x) \quad (7.8)$$

Where

$$\Theta(x) = \begin{cases} 1 & x \geq 0 \\ 0 & x < 0 \end{cases} \quad (7.9)$$

and $\mu_n = \sqrt{k^2 - \left(\frac{n\pi}{l}\right)^2}$

Denoting

$$M_n(x) \equiv \sqrt{\frac{2-\delta_{n0}}{l}} \cos \frac{n\pi}{l} x \quad (7.10)$$

Eq.(7.8) can be rewritten as

$$E_x^- = \sum_{n=0}^{\infty} C_n^r M_n(x) \sin[\mu_n(z+h)] \Theta(x) \Theta(l-x) \quad (7.11)$$

The continuity of E_x at $z=0$ yields

$$R_r(x,0) + \sum_{p=-\infty}^{+\infty} S_p^r R_p(x,0) = \sum_{n=0}^{\infty} C_n^r M_n(x) \sin(\mu_n h) \Theta(x) \Theta(l-x) \quad (7.12)$$

Multiplying both sides with $\overline{R_p(x,0)}$ and integrating over x on the range of x from $0 \rightarrow L$ yields

$$\begin{aligned} \int \overline{R_p(x,0)} R_r(x,0) dx + S_p^r &= \sum_{n=0}^{\infty} C_n^r \int \overline{R_p(x,0)} M_n(x) dx \sin(\mu_n h) \Theta(x) \Theta(l-x) \\ \delta_{rp} + S_p^r &= \sum_{n=0}^{\infty} C_n^r I_n^p \sin(\mu_n h) \end{aligned} \quad (7.13)$$

$$\begin{aligned} I_n^p &= \int \overline{R_p(x,0)} M_n(x) \Theta(x) \Theta(l-x) dx \\ &= \left(\frac{2-\delta_{n0}}{Ll} \right)^{\frac{1}{2}} [(-1)^n e^{-i\alpha_p l} - 1] \frac{i\alpha_p}{\alpha_p^2 - \left(\frac{n\pi}{l}\right)^2} \end{aligned} \quad (7.14)$$

Since

$$\begin{aligned} \nabla \times H &= \frac{\partial \vec{D}}{\partial t} = \epsilon \frac{\partial \vec{E}}{\partial t} = -i\omega\epsilon \vec{E} \\ \begin{vmatrix} \vec{i} & \vec{j} & \vec{k} \\ \frac{\partial}{\partial x} & \frac{\partial}{\partial y} & \frac{\partial}{\partial z} \\ H_x & H_y & H_z \end{vmatrix} &= -i\omega\epsilon E_x \vec{i} \\ i \left(\frac{\partial H_z}{\partial y} - \frac{\partial H_y}{\partial z} \right) &= -i\omega\epsilon E_x \vec{i} \end{aligned}$$

Since $H_z=0$, we get

$$H_y = i\omega\epsilon \int E_x dz \quad (7.15)$$

For $z>0$:

$$\begin{aligned}
H_y &= \left[\frac{1}{\sqrt{L}} e^{i\alpha_r x} \frac{e^{-i\beta_r z}}{-i\beta_r} + \sum_{p=-\infty}^{\infty} s_p^r \frac{1}{\sqrt{L}} e^{i\alpha_p x} \frac{e^{i\beta_r z}}{i\beta_r} \right] (i\epsilon w) \\
&= \left[R_r(x, z) \frac{1}{-i\beta_r} + \sum_{p=-\infty}^{\infty} s_p^r R_p(x, z) \frac{1}{i\beta_p} \right] (i\epsilon w)
\end{aligned} \quad (7.16a)$$

For $z < 0$:

$$\begin{aligned}
H_y &= \left[\sum_{n=0}^{\infty} C_n^r \sqrt{\frac{2 - \delta_{n0}}{l}} \cos \frac{n\pi}{l} x \int \sin[\mu_n(z+h)] dz \right] (i\epsilon w) \\
&= \sum_{n=0}^{\infty} C_n^r M_n(x) \frac{\cos[\mu_n(z+h)]}{-\mu_n} (i\epsilon w)
\end{aligned} \quad (7.16b)$$

at $z=0$, we have

$$H_y^+ = \left[-R_r(x, 0) \frac{k}{\beta_r} + \sum_{p=-\infty}^{\infty} s_p^r R_p(x, 0) \frac{k}{\beta_p} \right] (cn) \quad (7.17a)$$

$$H_y^- = \left[-\sum_{n=0}^{\infty} C_n^r M_n(x) \cos \mu_n h \frac{ik}{\mu_n} \right] (cn) \quad (7.17b)$$

The continuity of H_y at $z=0$ yields

$$-R_r(x, 0) \frac{k}{\beta_r} + \sum_{p=-\infty}^{\infty} s_p^r R_p(x, 0) \frac{k}{\beta_p} = -\sum_{n=0}^{\infty} C_n^r M_n(x) \cos \mu_n h \frac{ik}{\mu_n} \quad (7.18)$$

Substituting Eq.(7.13) into Eq.(7.18) yields

$$\begin{aligned}
&-R_r(x, 0) \frac{k}{\beta_r} - R_r(x, 0) \frac{k}{\beta_r} + \sum_{p=-\infty}^{+\infty} \sum_{n=0}^{\infty} C_n^r I_n^p \sin(\mu_n h) R_p(x, 0) \frac{k}{\beta_p} = -\sum_{n=0}^{\infty} C_n^r M_n(x) \cos \mu_n h \frac{ik}{\mu_n} \\
&\sum_{n=0}^{\infty} C_n^r M_n(x) \cos \mu_n h \frac{ik}{\mu_n} + \sum_{n=0}^{\infty} \sum_{p=-\infty}^{\infty} C_n^r I_n^p \sin(\mu_n h) R_p(x, 0) \frac{k}{\beta_p} = 2R_r(x, 0) \frac{k}{\beta_r}
\end{aligned}$$

Multiplying both sides with $\overline{M_n(x)}$ and integrating over x yields:

$$C_n^r \cos \mu_n h \frac{ik}{\mu_n} + \sum_{n=0}^{\infty} \sum_{p=-\infty}^{\infty} C_n^r I_n^p \sin(\mu_n h) \overline{I_n^p} \frac{k}{\beta_p} = 2 \frac{k}{\beta_r} \overline{I_n^0} \quad (7.19)$$

i.e.,

$$\sum_{N=0}^{\infty} \left\{ i \frac{k}{\mu_N} \cos \mu_N h \delta_{Nn} + \left(\sum_{p=-\infty}^{\infty} \frac{k}{\beta_p} I_N^p \overline{I_N^p} \right) \sin \mu_N h \right\} C_N^r = 2 \frac{k}{\beta_r} \overline{I_n^0} \quad (7.20)$$

$$I_z = \frac{1}{2} \text{Re}(\vec{E} \times \vec{H})_z \quad (7.21)$$

As soon as we know the intensity of electromagnetic field at any point along z direction, the quantum efficiency of QWIP+photonic crystal can be obtained.

7.3 Results and Discussion

7.3.1 Transmission Coefficient of a Photonic Crystal Structure

Figure 7.3 shows the transmission coefficient of a GaAs/AlAs multi-layer structure. The incident photon wavelength under consideration is $9.4 \mu\text{m}$. In figure 7.3 (a) and (b), the period number is 15 and 30, respectively. In figure 7.3 (c) and (d), a defect (by doubling the thickness of the middle AlAs layer) is added to the structure, the period number at the both sides of the defect is 15 and 30, respectively in figure 7.3 (c) and (d).

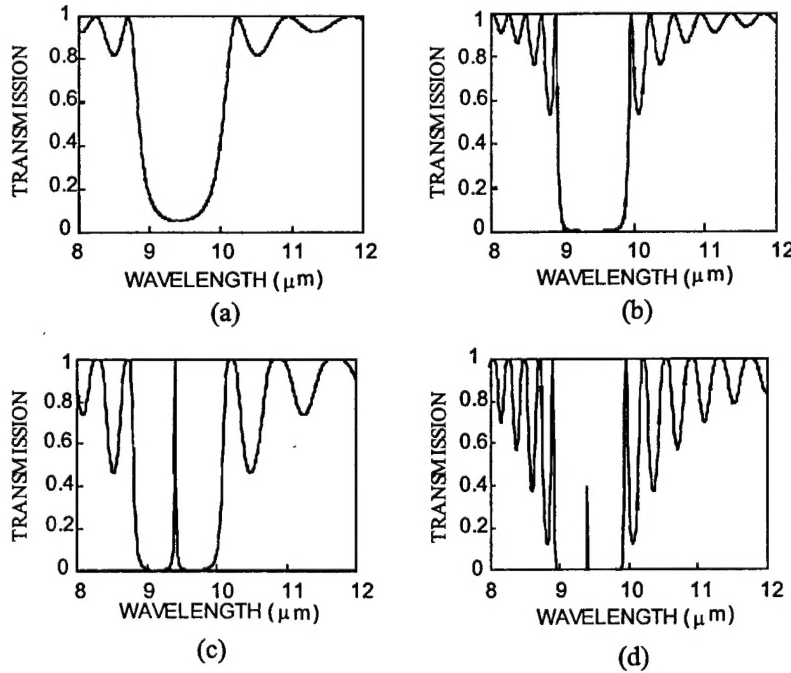


Figure 7.3 Transmission coefficient of a GaAs/AlAs multi-layer structure.

It can be seen from figure 7.3 (a) and (b) that a photonic gap does exist in this multi-layer structure. With the increase of period number, the gap will become sharper. If a defect (in this case we double the thickness of the middle AlAs layer) is placed in the structure, a defect mode will be created and photon at this frequency can enter this structure.

8. Publications

1. M.Z. Tidrow, Xudong Jiang, Sheng S. Li and K. Bacher, "A Four-color Quantum Well Infrared Photodetector", invited talk, *6th International Symposium on Long Wavelength Infrared Detectors and Arrays*, Boston, Nov. 5-6, 1998.
2. M. Z. Tidrow, X. D. Jiang, Sheng S. Li, and K. Bacher, "A Four-color Quantum Well Infrared Photodetector", *Appl. Phys. Lett.* **74**,1335 (1999).
3. Xudong Jiang, Sheng S. Li and M. Z. Tidrow, "Investigation of A Multi-Stack Voltage-Tunable Four-Color Quantum Well Infrared Photodetector for Mid- and Long-Wavelength Infrared Detection", *IEEE Journal of Quantum Electronics* **35**, 1685 (1999).
4. Xudong Jiang, Sheng S. Li and M.Z. Tidrow, "Study on the Intersubband Transitions in Quantum Dots and Quantum Dot Infrared Photodetectors", *Physica E* **5**, 27 (1999).
5. Meimei Z. Tidrow, Xudong Jiang, Sheng S. Li, Junhee Moon and W.K. Liu, "Very Long Wavelength Quantum Well Infrared Photodetectors," presented at the 196th Meeting of the Electrochemical Society, *Electrochemical Society Proceedings* 99-22, 447 (1999).
6. Jung-Hee Lee, Sheng S. Li, M. Z. Tidrow, W. K. Liu and K. Bacher, "Quantum Well Infrared Photodetectors With Digital Graded Superlattice Barrier for Long Wavelength and Broadband Detection", presented at the 196th Meeting of The Electrochemical Society, *Electrochemical Society Proceedings* 99-22, 436 (1999).
7. Meimei Z. Tidrow, Xudong Jiang, Sheng S. Li, Junhee Moon, W.K. Liu and K. Bacher, "Very-Long-Wavelength Quantum Well Infrared Photodetectors," presented at the 8th Annual AIAA/BMDO Technology Conference, July 19-22, 1999 at MIT Lincoln Laboratory in Lexington, MA.

8. Jung-Hee Lee, Sheng S. Li, M. Z. Tidrow, W. K. Liu and K. Bacher, "Quantum Well Infrared Photodetectors With Digital Graded Superlattice Barrier for Long Wavelength and Broadband Detection," *Appl. Phys. Lett.* **75**, 3207 (1999).
9. Jung-Hee Lee, Sheng S. Li, M. Z. Tidrow, and W. K. Liu, ". High- sensitivity Quantum Well Infrared Photodetectors With linear Graded Barrier," submitted to *Electronics Letters*, April, 2000.
10. Jung Hee Lee, Sheng S. Li, and M. Z. Tidrow, "Multicolor, Broadband Quantum Well Infrared Photodetectors Using Digital Graded Superlattice Barrier and Linear-graded Barrier for LWIR Detection," to be presented at the International QWIP 2000 Workshop, Dana Point, CA, July 27-30, 2000.